THE JOURNAL OF PHYSICAL CHEMISTRY C

pubs.acs.org/JPCC Article

Characterizing Complex Gas−Solid Interfaces with in Situ Spectroscopy: Oxygen Adsorption Behavior on Fe−N−C Catalysts

Michael J. Dzara, Kateryna Artyushkova, Moulay Tahar Sougrati, Chilan Ngo, Margaret A. Fitzgerald, Alexey Serov, Barr Zulevi, Plamen Atanassov, Frédéric Jaouen, and Svitlana Pylypenko*

Cite This: J. Phys. Chem. C 2020, 124, 16529−16543 Read Online

ACCESS | Metrics & More | Article Recommendations | Supporting Information

ABSTRACT: Electrocatalysts for the oxygen reduction reaction within polymer electrolyte membrane fuel cells based on iron, nitrogen, and carbon elements (Fe−N−C) have received significant research attention as they offer an inexpensive alternative to catalysts based on platinum-group metals. Although both the performance and the fundamental understanding of Fe−N−C catalysts have improved over the past decade, there remains a need to differentiate the relative activity of different active sites. Toward this goal, our study is focused on characterizing the interactions between O_2 and a set of five structurally different Fe−N−C materials. Detailed characterization of the Fe speciation was performed with ^{57}Fe Mössbauer spectroscopy and soft X-ray absorption spectroscopy of the Fe $L_{3,2}$-edge, whereas nitrogen chemical states were investigated with X-ray photoelectron spectroscopy (XPS). In addition to initial sXAS and XPS measurements performed in ultra-high vacuum (UHV), measurements were also performed (at the identical location) in an atmosphere of 100 mTorr of O_2 at 80 °C (O_2-rich). XPS and sXAS results reveal the presence of several types of FeN_xC_y adsorption sites. FeN_xC_y sites that are proposed as the most active ones do not show significant change (based on the techniques used in this study) when their environment is changed from UHV to O_2-rich. Correlation with Mössbauer and sXAS results suggests that this is most likely due to the persistence of strongly adsorbed O_2 molecules from their previous exposure to air. However, other species do show spectroscopic changes from UHV conditions to O_2-rich. This implies that these sites have a weaker interaction with O_2 that results in their desorption in vacuum conditions and re-adsorption when exposed to the O_2-rich environment. The nature of these weakly and strongly O_2-adsorbing FeN_xC_y sites is discussed in the context of different synthetic and processing parameters employed to fabricate each of these five Fe−N−C materials.

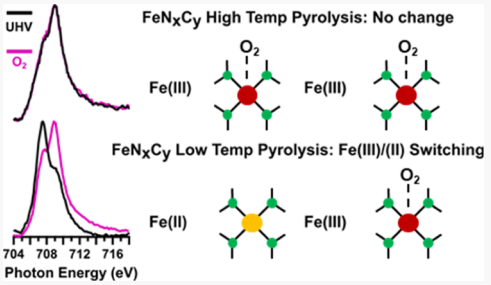

1. INTRODUCTION

Significant research effort has been put toward the development of cost-effective, high-performance electrocatalysts for the oxygen reduction reaction (ORR) with the goal of enabling widespread commercial adoption of polymer electrolyte membrane fuel cells (PEMFCs) as a carbon emission-free energy conversion device.[1,2] While many promising catalysts are based upon nanostructured platinum group metal (PGM) elements and alloys,[3−8] PGM-free alternatives—particularly those based on high surface area iron and nitrogen-functionalized carbon (Fe−N−C) structures—have become increasingly competitive over the past decade.[9−11] The Fe−N−C family of catalysts is inherently complex because of the multitude of bonding states available for nitrogen and carbon and the structural/morphological heterogeneity of high surface area carbons.[12] Additionally, their complexity is further compounded by the use of various synthetic approaches to form highly active Fe−N−C catalysts, often involving multiple steps and utilizing different iron, nitrogen, and carbon sources.[11,13−17] This typically results in the presence of multiple potential active sites, including defective carbon, various nitrogen−carbon (NC) species, and Fe-based sites that can be described as FeN_xC_y moieties formed by covalent bonding of atomically dispersed iron ions to 2−4 nitrogen atoms within the carbon matrix.[12,18,19] While FeN_xC_y moieties, particularly those where $x = 4$, are frequently suggested in the literature to be the most active site, the debate continues on the exact nature of the most active site, the impact of different C and NC sites on overall fuel cell performance, and the relative activity of the different FeN_xC_y structures. Therefore, it is necessary to attempt to separate the contributions of the various possible active sites to the ORR to further optimize these catalysts by increasing the density of the most active sites while also decreasing the density of species detrimental to fuel cell performance.[18,20,21]

Analysis of Fe−N−C catalysts necessitates in-depth characterization combining multiple techniques that provide

Received: June 9, 2020
Revised: June 30, 2020
Published: July 1, 2020

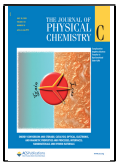

https://dx.doi.org/10.1021/acs.jpcc.0c05244
J. Phys. Chem. C 2020, 124, 16529−16543

information at multiple scales. A selection of the most commonly featured techniques includes (but is not limited to) transmission electron microscopy (TEM) and energy-dispersive X-ray spectroscopy (EDS) to evaluate the morphology and spatially resolved elemental dispersion, electron energy loss spectroscopy to identify atomically dispersed iron species, X-ray absorption spectroscopies (XAS) for evaluation of iron and nitrogen coordination and iron oxidation state, X-ray photoelectron spectroscopy (XPS) primarily to identify different surface nitrogen and carbon speciation, and ^{57}Fe Mössbauer spectroscopy for the identification of differences in iron coordination and oxidation state, electronic properties, and spin state.[22−25] Although each technique has its own strengths and weaknesses, it is possible to draw robust correlations with synthesis parameters and/or electrochemical testing results by combining several of the above techniques, along with other complementary characterization as needed. Additionally, complementing characterization with theoretical calculations or designing model materials with systematically controlled properties has been used effectively to add further clarity to a characterization study.[26−30]

Experimental differentiation of the various FeN_xC_y sites has primarily been done with ^{57}Fe Mössbauer spectroscopy, quite often in conjunction with XAS and computations.[25,26,31] Even within Fe−N−C catalysts free or quasi-free of Fe clusters, two or more distinct iron species in an FeN_xC_y-type configuration are ubiquitously identified.[26,31−33] Within ^{57}Fe Mössbauer spectroscopy-based studies, a particular quadrupole doublet (usually referred to in the literature, and herein, as D1) has been shown to correlate with catalytic activity.[34,35] However, it has remained a challenge to unambiguously assign the precise stoichiometry, oxidation state, and spin state of this FeN_xC_y moiety. Until recently, D1 has most often been assigned to Fe(II) with no spin (S = 0) or Fe(III) in a high spin (S = 5/2) state.[34,36−38] However, two recent studies by Wagner et al. and Mineva et al. have provided substantial evidence highlighting the complexity of definitively assigning the D1 feature and proposed alternative physicochemical interpretations.[26,39] The results of Wagner et al.'s work suggest that D1 collected by room-temperature (RT) ^{57}Fe Mössbauer spectroscopy with no applied magnetic field may be convoluted by overlapping signals from very small (<3 nm) clusters of iron oxide. Additionally, the portion of the D1 signal still assigned to an FeN_4 species was found to consist of neither pure ferrous nor ferric character but rather a mixture of oxidation states.[39] This result had previously been postulated to be caused by O_2 adsorption on FeN_xC_y sites, resulting in a change in the oxidation state of the Fe(II) center to Fe(III),[32,40−42] a hypothesis the authors also suggest. Mineva et al.'s recent study supplies a thorough argument, suggesting that the highly active FeN_xC_y sites attributed to the D1 signal have a $Fe(III)N_4C_{12}$ structure with high spin. The authors hypothesize that this can be attributed to the presence of an adsorbed O_2 molecule at the iron center. In turn, they additionally proposed that this differentiates surface sites (gas-phase accessible) from those present within the bulk of the catalyst (gas-phase inaccessible) which remains in all conditions in an Fe(II) state (quadrupole doublet component with high quadrupole splitting of ca. 2.4−2.7 mm s^{-1}, usually labeled D2 in the literature). Another possible explanation is that D1 and D2 differentiate the surface sites with strong oxygen binding (D1 component) from other surface sites with weaker oxygen binding (D2, or a fraction of D2 signal). Surface sites with a sufficiently high Fe(III)/Fe(II) redox potential would be in an Fe(II) state at open-circuit conditions and may bind O_2 more weakly and also reversibly.[26] These recent advances in the understanding of the nature of FeN_xC_y species and the complexity in characterizing and analyzing their differences have significant implications to both the catalyst design and interpretation of characterization results and motivate further characterization studies focused on understanding FeN_xC_y sites and their interactions with O_2.

Accessing the catalyst−O_2 interface is of particular interest in order to definitively identify which species interact with O_2 and to what extent. The strength of the interaction between an FeN_xC_y site and O_2 has been suggested to correlate with ORR activity and may follow a Volcano-type relationship where an optimal "not too strong, not too weak" interaction is ideal.[43] Both ^{57}Fe Mössbauer spectroscopy and XAS do not have ultra-high vacuum (UHV) requirements (although certain instrumental configurations may enable such experiments) and therefore, when operated at ambient conditions, may preserve the existing interactions of FeN_xC_y surface sites with O_2 from the air and/or enable studies in a controlled environment targeted at understanding interactions with O_2. Indeed, several XAS studies on Fe−N−C catalysts under applied potentials (at the Fe K-edge, in N_2- or O_2-saturated electrolyte) have identified that the potential that Fe(III)/Fe(II) switching occurs at correlates with a catalyst's activity.[29,40,44] However, both ^{57}Fe Mössbauer spectroscopy and XAS are bulk techniques that, depending on the Fe−N−C material, may contain a majority of contributions from Fe species that are inaccessible by gas phase or liquid electrolyte. Utilizing near-ambient pressure XPS (nAP-XPS) instruments enables in situ measurements (in this work in situ refers to measurement in the presence of one or more external stimuli, e.g., elevated temperature, applied potential, or controlled gaseous environments, not during device operation) at pressures ranging from hundreds of mTorr to tens of Torr, making the gas−solid interface in Fe−N−C catalysts accessible for study.[45−47] The majority of nAP-XPS catalyst−gas interaction studies investigate crystalline films of metals or metal oxides,[48−51] and only a few recent studies have reported the characterization of complex interactions between oxygen and high surface area NC and Fe−N−C materials.[52,53] This may be due in part to several challenges associated with nAP-XPS measurements of the NC/Fe−N−C catalyst−O_2 interface. Because of the very low density of FeN_xC_y sites present in Fe−N−C catalysts (typically near or below 1 at. %), and the inherent complexity associated with analyzing changes in the oxidation state in Fe 2p core-level XP spectra because of multiplet splitting,[54] it is exceedingly difficult to analyze the changes in FeN_xC_y species through measurement of the Fe 2p narrow scan spectrum using nAP-XPS. Although signal due to FeN_xC_y species may still be accessed through analysis of the N 1s core level, contributions from other N-groups in NC that are not engaged in the coordination of Fe cations will also be present and their corresponding shifts must also be accounted for. Recently, adsorption of O_2 to hydrogenated nitrogen, electron-rich nitrogen species, and graphitic nitrogen species was isolated within a sample set of NC materials produced through different synthetic routes through the use of spectral subtraction,[52] providing a methodology for a similar analysis of changes in the N 1s due to catalyst−O_2 interactions on Fe−N−C catalysts in an attempt to isolate O_2 adsorption to

https://dx.doi.org/10.1021/acs.jpcc.0c05244
J. Phys. Chem. C 2020, 124, 16529−16543

FeN_xC_y species. This type of measurement can be effectively complemented by conducting XAS measurements using a soft X-ray source (sXAS) of the Fe L-edge in total electron yield (TEY) mode. Such a configuration results in a surface-sensitive measurement with an information depth on the order of several nanometers, similar to that achieved by XPS.[55] While Fe L-edge sXAS has been performed (both ex situ and in situ) on a diverse set of Fe-based samples for a variety of applications,[56−58] it has not been commonly applied to Fe−N−C-type ORR catalysts. However, a study on Fe-CNT-GN hybrid materials that features sXAS of the Fe L-edge under UHV did identify the presence of an $Fe(III)N_x$-type species, and through confirmation with the O K-edge, attributed the presence of the Fe(III) species to an adsorbed O_2 molecule on the iron center.[41] An in situ sXAS study focused on O_2 and H_2 exposure of Co- and Fe-phthalocyanine macromolecular catalysts found evidence for an increase in the ratio of Fe(III)/Fe(II) upon exposure to O_2, whereas restricted changes in the spectra for Co suggested a retained Co(II) oxidation state.[42] Therefore, it is evident that using both nAP-XPS and sXAS of the Fe L-edge, it is possible to conduct a robust in situ experiment with surface-sensitive measurement of both nitrogen and iron species to determine how they evolve when switching from an O_2-free to an O_2-rich gaseous environment.

This work presents the first in situ study of O_2 interactions with Fe−N−C catalysts featuring measurement of both the N 1s core level by nAP-XPS and the Fe L-edge by sXAS, capturing surface-sensitive data that is both nitrogen atom specific and iron atom specific on the same area of analysis and with the same temperature and pressure conditions. This unique approach is enabled by the capabilities at end-station 11.0.2 of the advanced light source (ALS) user facility, described in detail elsewhere.[59,60] The different O_2 interactions are related to physicochemical properties such as morphology, spatial elemental distribution, initial nitrogen chemistry, and initial iron properties, which were thoroughly characterized by ^{57}Fe Mössbauer spectroscopy, (S)TEM/EDS, UHV XPS, and UHV sXAS. The sample set of Fe−N−C materials was carefully selected to include both highly active catalysts and model high surface area structures. The highly active catalysts include an Fe−N−C material derived from a sacrificial Zn-based imidazolate (ZIF-8) metal−organic-framework (MOF) and a templated material based on the sacrificial-support-method (SSM).[10,32,61] Model Fe−N−C structures based on nanospherical particles (herein referred to as NS-i, where i is 1, 2, or 3 depending upon the exact synthetic process, described in Section 2.1.1) on the order of 150−250 nm in diameter were produced by several variations of a previously reported hydrothermal synthesis.[27,52,62,63] This work provides evidence that (i) different NC and FeN_xC_y sites may show different strengths of interactions with oxygen and (ii) some sites are typically more accessible for adsorption than others (e.g., D1 vs D2). Specifically, some FeN_xC_y sites have a strongly adsorbed O_2 molecule (which remains on the catalyst surface even during UHV measurements) that results in an Fe(III) center for the fraction of such sites that is accessible for gas-phase adsorption, whereas other FeN_xC_y sites as well as NC functional groups adsorb O_2 less strongly, leading to O_2 desorption in UHV conditions and O_2 re-adsorption at 100 mTorr of O_2 pressure.

2. METHODS

2.1. Materials Synthesis. *2.1.1. Solvothermal Synthesis of Fe−N−C Nanospheres.* A solvothermal synthetic scheme previously reported for the production of NC NS was adapted to synthesize Fe−N−C NS samples.[27,52,62,63] The samples featured in this study were produced by two variations of the following procedure: in the first method, the Fe precursor is added in the first step, prior to the formation of the spherical NC particles (designated 1-HT as there is only a single heat treatment), whereas the second method introduces the Fe precursor in a separate process after the preparation of the NC NS (2-HT). For both syntheses, an aqueous alcohol solution was first prepared by mixing 320 mL of 18.2 MΩ deionized (DI) H_2O and 128 mL of ethanol (Pharmco-Aaper, high-performance liquid chromatography grade) in a 1 L high-density polyethylene bottle. Then, 3.2 g of resorcinol (Sigma-Aldrich, >99%) was dissolved while stirring at 300 RPM. Once fully dissolved, 5.4 mL of ethylenediamine (Sigma-Aldrich, >99.5%) was dissolved in solution, followed by 4.8 mL of 37 wt % formaldehyde (Alfa Aesar, 36.5−38%). Finally, in the case of the 1-HT Fe−N−C spheres, an aliquot of Fe(II) acetate tetrahydrate (Sigma-Aldrich, 99%) was added such that the mass of Fe was 5 wt % of the total precursor mass. The solution was stirred at RT for 24 h; then, the bottle was sealed with Durafilm and heated in an oven at 100 °C for 24 h. After cooling the vessel, the product was isolated via centrifugation at 9327 G for 20 min and then transferred to a quartz boat and dried for 12 h. After drying, the product was pyrolyzed in a Lindberg Blue-M tube furnace under flowing N_2 by heating at 2 °C/min up to 350 °C, dwelling for 4 h, then heating at 5 °C/min up to 600 °C, and dwelling for 2 h, resulting in either the final product in the case of sample NS-1 or finished NC NS for use in the synthesis of NS-2 and NS-3.

The second step of the 2-HT synthesis was started by dispersing 200 mg of NC NS and an amount of Fe precursor such that the mass of Fe is 5 wt % in 200 mL of methanol (Pharmco-Aaper, Reagent Grade) in a 500 mL round-bottom flask. The Fe precursors used were either Fe(II) acetate tetrahydrate (Sigma-Aldrich, 99%) in the case of NS-2 or Fe(III) Cl_3 hexahydrate (Sigma-Aldrich, >98% Reagent Grade) for NS-3. The dispersion was then sonicated for 90 min. A rotary evaporator was used at 60 °C and ∼350 mbar in order to remove the solvent. The resulting powder was pyrolyzed in a Lindberg Blue-M tube furnace under flowing N_2 at 700 °C for 4 h. The temperature was ramped to 700 °C at a rate of 3 °C/min and allowed to cool at 5 °C/min, resulting in a fine black powder.

2.1.2. MOF Fe−N−C Synthesis. The synthesis of the ZIF-8 derived Fe−N−C material (labelled MOF-$Fe_{0.5}$) was first reported by Zitolo et al.[32] The synthesis involves the dry ball-milling of the three precursors, namely, ZIF-8 (Basolite Z1200 from BASF), Fe(II) acetate, and 1,10-phenanthroline (Phen—Sigma-Aldrich), followed by a single pyrolysis in flowing argon. The first step of the synthesis involved the dry ball-milling of ZIF-8 (800 mg), Phen (200 mg), and Fe(II) acetate (16 mg) in a zirconium oxide crucible filled with 100 zirconium oxide balls (5 mm diameter) in a planetary ball miller (Fritsch Pulverisette 7 Premium, Fritsch, Idar-Oberstein, Germany). The milling was performed at 400 rpm for a total duration of 2 h, split in four cycles of 30 min each, with resting time in between to avoid heating. The catalyst precursor contains 0.5 wt % Fe, explaining the subscript in the catalyst label, MOF-

https://dx.doi.org/10.1021/acs.jpcc.0c05244
J. Phys. Chem. C 2020, 124, 16529−16543

$Fe_{0.5}$. The catalyst precursor following the ball-milling was collected as such and was pyrolyzed in flash mode in Ar at 1050 °C for 1 h. The flash mode indicates that the oven was preheated at 1050 °C for 1.5 h, and then the quartz boat and catalyst precursor were pushed inside the heating zone with an outer magnet.[64] The catalyst precursor powder experiences an increase in temperature from RT to 1050 °C within circa 45 s, and the pyrolysis is then continued for 1 h, after which the split hinge oven is opened and the quartz tube is immediately removed and let to cool down in ambient atmosphere, still with flowing Ar in the tube. Once cooled down, the tube is opened and the catalyst collected. No other step is applied. It is important to note that, owing to a mass loss of 65−70 wt % during pyrolysis in Ar caused by volatile products formed from ZIF-8 and Phen, the bulk iron content in $Fe_{0.5}$ is about 3 times the iron content in the catalyst precursor, circa 1.5 wt % Fe.

2.1.3. SSM Fe−N−C Synthesis. The catalyst was synthesized by modified SSM[61] practiced at Pajarito Powder, LLC as a VariPore method. Iron nitrate [2.5 g, $Fe(NO_3)_3{\cdot}9H_2O$, Sigma−Aldrich] was mechanically mixed with 25 g of the nitrogen-rich organic precursors (Pipemidic acid) and 10 g of LM-150 fumed silica (Cabot Cab-O-sil, surface area ∼150 m^2/g). The homogeneous powder was dried at a temperature of 80 °C for 8 h and pyrolyzed at 950 °C for 55 min in flowing ultrahigh purity (UHP) nitrogen, 100 ccm. After heat treatment, silica was removed by 20 wt % HF (1st acid treatment), followed by washing with DI water until neutral pH was reached. The obtained powder was dried overnight at 85 °C. In order to remove Fe metallic particles, the catalysts were acid treated with 1 M HNO_3 (2nd acid treatment). Additional heat treatment was done in a UHP nitrogen atmosphere at a temperature of 1000 °C for 45 min.

2.2. Microscopy. STEM−EDS was conducted using a FEI Talos F200X operated at 200 kV. Samples were prepared by brushing Cu grids with holey carbon support films through the powders. Elemental EDS maps at various magnifications were acquired for up to 30 min per area, and data were both collected and processed by standard methods using Bruker ESPRIT software.

2.3. ^{57}Fe Mössbauer Spectroscopy. All spectra were acquired ex situ at RT and in ambient air, and the Fe−N−C materials had also been exposed to air since their synthesis. The ^{57}Fe Mössbauer spectrometer (Wissel, Germany) was operated in transmission mode with a ^{57}Co:Rh source. The velocity driver was operated in constant acceleration mode with a triangular velocity waveform. The velocity scale was calibrated with the magnetically split sextet of a high-purity α-Fe foil at RT. The spectra were fitted by the least-squares method to appropriate combinations of Lorentzian profiles representing quadrupole doublets, sextets, and singlets. The values of isomer shifts (IS) are reported relative to α-Fe foil at RT.

2.4. UHV- and nAP-XPS, sXAS. Synchrotron facilities at beamline 11.0.2 were used to collect all XPS and sXAS data shown.[59,60] Samples were dispersed in isopropyl alcohol and drop-cast onto a conducting gas-diffusion-electrode carbon paper. All samples were first measured at RT under UHV (<1 × 10^{-8} Torr). High-resolution C 1s, O 1s, and N 1s spectra were collected with photon energies of 490, 735, and 600 eV such that the kinetic energy of ejected photoelectrons would be roughly the same. A pass energy of 100 eV was used, excluding the N 1s, which had a pass energy of 50 eV. The same measurement settings were used to acquire data under in situ conditions (100 mTorr O_2) at a temperature of 80 °C, and also 100 mTorr each of O_2 and H_2O vapor, also at 80 °C. For the humidified O_2 atmosphere, H_2O vapor was added after O_2-only measurements were already taken, and thus, the two gases were added sequentially (O_2, then H_2O), not simultaneously. In situ measurements were performed on the same area of analysis with the same focal distance as the initial UHV measurements to reduce the impact of sample heterogeneity. Energy calibration of XP spectra was performed by collecting the Au 4f region at UHV and RT of a gold metal contact present as part of the sample holder at each PE used. Correction to 83.95 eV was used, and then the BE difference was applied to each environment through the C 1s which showed no appreciable change in spectral features. C 1s data are shown for calibration validation in Figure S1. For spectral subtraction, background-subtracted (a linear background was used) spectra were normalized by total peak area before subtraction to account for differences in photoelectron intensity because of attenuation in the O_2 atmosphere measurements. Data collected at UHV were subtracted from the O_2 atmosphere data.

sXAS at the Fe L-edge was also collected at beamline 11.0.2 with the detector in TEY mode, at the same pressure and temperature combinations as the nAP-XPS data, and on the same position of analysis on the sample.

3. RESULTS

3.1. Characterization of Materials under UHV Conditions: STEM−EDS, XPS, and sXAS. The materials used in this study were carefully selected to represent a variety of common catalyst structures with different Fe and N species present. Two samples (MOF-$Fe_{0.5}$ and SSM) represent highly active Fe−N−C catalysts with different structures: one derived from a sacrificial MOF (ZIF-8) used to prepare a highly microporous N-doped carbon matrix and the other a mesoporous, templated material based on the sacrificial support method (SSM). Both have been the subject of prior rigorous studies investigating ORR performance and relating the performance to physicochemical properties.[10,21,32,61,65−67] The other three samples are based on microporous NS particles produced by variations of a solvothermal synthesis method.[27,52,62,63] These three materials were designed to model different Fe species often found in Fe−N−C catalysts (e.g., discrete particles vs. atomically dispersed Fe cations) while attempting to maintain very similar size, shape, morphological properties, and distribution of nitrogen species. Across the sample set, one of the most significant differences in sample preparation is the pyrolysis temperature the samples are exposed to. A recent study has shown that FeN_4-type bonding forms as low as 400 °C.[68] It is also well documented that further evolution of the carbonaceous matrix, including increased graphitization, occurs at higher temperatures—often resulting in significantly improved ORR activity compared to low-temperature pyrolyzed materials.[18,68] Indeed, many highly active Fe−N−C catalysts (including MOF-$Fe_{0.5}$ and SSM) are pyrolyzed at much higher temperatures, usually in excess of 900 °C.[10,21,32,61,65] Conversely, the NS samples were all pyrolyzed at lower temperatures of either 600 °C (NS-1) or 700 °C (NS-2 and NS-3). This difference in temperature is likely to impact the localized structure of the carbon surrounding a possible FeN_xC_y active site and could result in different O_2 adsorption behavior. Therefore, differences in structure, morphology, and Fe and N speciation resulting from

https://dx.doi.org/10.1021/acs.jpcc.0c05244
J. Phys. Chem. C 2020, 124, 16529−16543

the different synthetic and processing parameters the samples experiences are first investigated with ex situ characterization techniques.

Figure 1 shows STEM bright-field (BF) images alongside EDS maps specific to C, N, and Fe for the three samples with

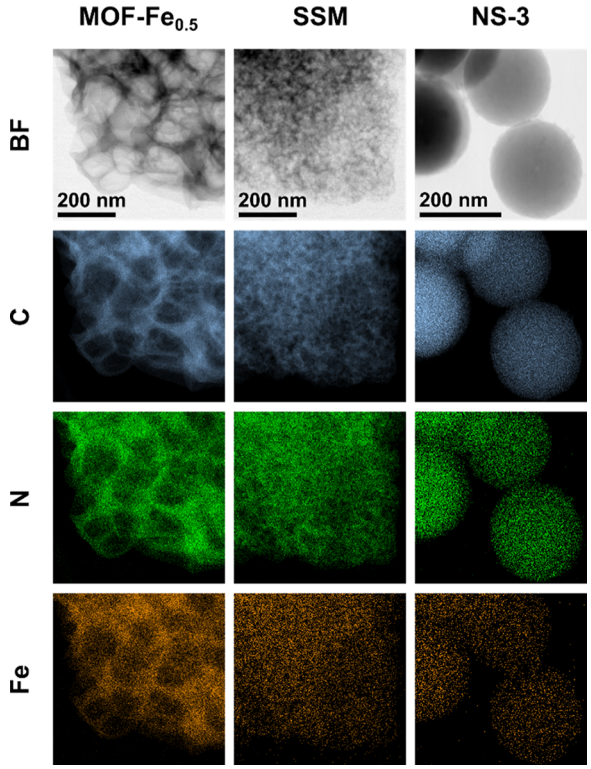

Figure 1. BF-mode (S)TEM images and C-, N-, and Fe-specific EDS maps are displayed for the MOF-$Fe_{0.5}$, SSM, and NS-3.

the most differences in morphology, highlighting their main differences and the range of studied structures. The MOF-$Fe_{0.5}$ sample has the most open structure, with a high specific surface area mostly from micropores with some contribution from narrow mesopores.[21] SSM has relatively smaller structural features and is known to contain a bimodal pore size distribution because of the controlled size of pore-formers.[10,61] NS-3 shows the typical structure and morphology of the NS samples. This particular sample was selected to be displayed alongside MOF-$Fe_{0.5}$ and SSM as it also has a uniform Fe dispersion, while highlighting the major differences in overall structure of NS samples compared to the MOF-$Fe_{0.5}$ and SSM catalysts. The C specific EDS map of NS-3 shows a degree of texturing across the surface of the NS. This texturing is likely related to the porosity of the NS samples, as they have a bimodal pore size distribution and the texturing can be explained by the presence of both meso- and micropores.[62] All three Fe−N−C samples in Figure 1 show a relatively even distribution of C, N, and Fe. In these examples, all samples show highly dispersed Fe species and do not reveal the presence of Fe nanoparticles at this resolution. A comparison of the three different NS samples is displayed in Figure 2 to highlight their differences in iron distribution. All three NS samples displayed in Figure 2 have similar overall shape, size, and morphology, as can be seen in the high angle annular dark-field (HAADF) images. The EDS maps below also show similar N distribution for each sample, and both NS-1 and NS-

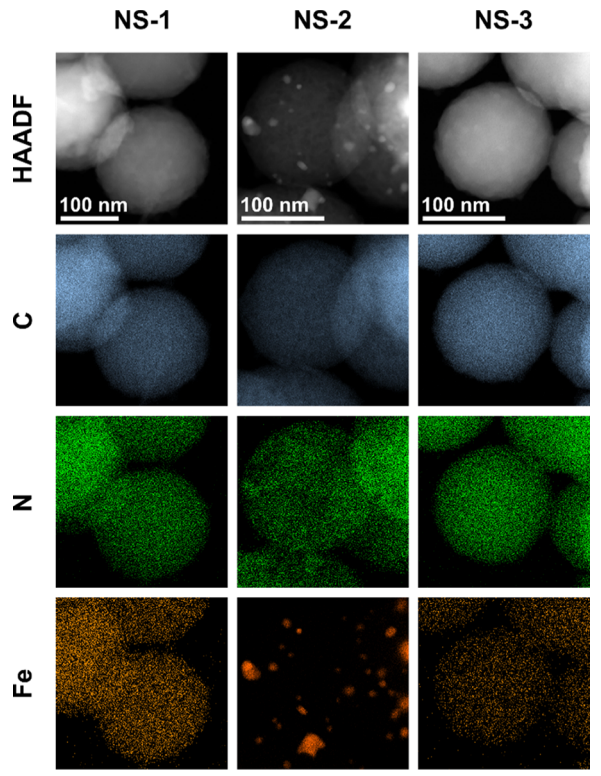

Figure 2. HAADF-mode TEM images and C-, N-, and Fe-specific EDS maps are displayed at high magnification for the three NS samples.

3 show a well-distributed signal for Fe, implying either only atomically dispersed Fe and/or (sub)nanosized particles, whereas NS-2 has Fe present in particle form (from single nanometers to tens of nanometers in diameter with no regular shape). Relative quantification of all samples from EDS is reported in Table 1. All five samples have very similar

Table 1. EDS Compositional Analysis

	C (at. %)	O (at. %)	N (at. %)	Fe (at. %)
MOF-$Fe_{0.5}$	93.5	3.0	3.1	0.4
NS-1	94.3	3.2	2.4	0.2
NS-2	96.7	1.1	0.7	1.2
NS-3	95.2	2.5	2.2	0.2
SSM	95.4	1.4	2.7	0.5

composition, with NS-2 displaying the largest amount of Fe and lowest amount of N due to the presence of Fe particles. Both NS-1 and NS-3 have less overall Fe and N content than the MOF-$Fe_{0.5}$ and SSM catalysts.

An analysis of the N 1s core level by XPS was performed in order to qualitatively examine the differences in N species present. Many studies in the literature featuring XPS data on Fe−N−C-based catalysts have employed curve-fitting of the N 1s core level in order to attempt to differentiate the various N species present, in which identifying FeN_xC_y moieties by the N atoms involved in the coordination of Fe cations is of particular interest. Such detailed information obtained from the N 1s fitting results is then often related to the ORR activity of catalysts.[13,19,27,52,53,63] However, curve-fitting and the subsequent assignment of components to N species are very complex because of the abundance of a variety of possible N

https://dx.doi.org/10.1021/acs.jpcc.0c05244
J. Phys. Chem. C 2020, 124, 16529−16543

moieties that may be present in an Fe−N−C catalyst. Additionally, the BE position of a particular N species can be impacted by local structural differences (e.g., edge effects and proximity of other dopant elements or defects in the C structure), which can cause shifts in the position of a species up to several eV in value.[69] Therefore, we display N 1s data without curve-fitting in order to highlight and compare the main features present in these samples (Figure 3). It is important to note that this data was collected with a lower photon energy ($h\nu$ = 600 eV) than typical, resulting in a photoelectron kinetic energy of ∼200 eV, circa 5 times lower than that of N 1s photoelectrons ejected upon exposure of a sample to the typical Al kα X-ray source. This does not necessarily mean that the N 1s data displayed in Figure 3 have exactly a 5× smaller information depth than classical XPS measurements because the relationship between photoelectron kinetic energy and information depth is complex.[70] However, we can safely assume that the lower photon energy measurements presented here are more surface sensitive than those typically reported in the literature. The N 1s spectra of all five samples show two distinct peaks at BE values between 400 and 398 and 402−400 eV, respectively. It is also clear, without any fitting, that the ratio of the two distinct peaks changes among the samples. While this certainly represents a simplified picture, each sample can be characterized as being predominantly comprised of either electron-rich, sp^2-type nitrogen species (pyridine, imine, and FeN_xC_y moieties), or sp^3-type hydrogenated nitrogen species (pyrrole, hydrogenated pyridine, and other protonated N species) by evaluating the relative abundance of these two main peaks. The MOF-$Fe_{0.5}$ and SSM samples represent the two extreme cases, as the MOF-$Fe_{0.5}$ sample contains the highest ratio of electron-rich nitrogen species to hydrogenated species, whereas the SSM sample contains the lowest ratio of electron-rich to hydrogenated species. The three NS samples present intermediate cases with a more balanced mix of electron-rich and hydrogenated species. NS-1 has nearly equal contribution from the two classes of nitrogen species. NS-2 and NS-3 have close to identical N 1s spectra, with greater relative contribution from hydrogenated species than electron-rich species. This is expected as it follows previous results on a set of metal-free NS in which pyrolysis temperature was shown to be the main variable impacting nitrogen chemistry.[52] It should be noted that the N 1s signal from FeN_xC_y moieties can be found at several different positions ranging from ∼400 to 398.5 eV depending on the exact configuration of the species and the local environment of the N atoms.[19,28,69,71] Because of the difficulty in definitively isolating these species and their typically low abundance relative to other N species, no attempt is made to differentiate FeN_xC_y species within the N 1s signal and we turn to Fe-specific characterization techniques to further interrogate such species.

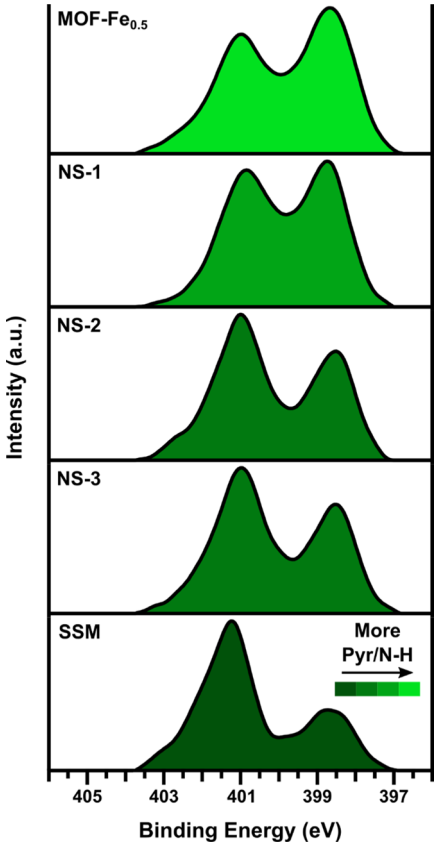

Figure 3. XPS N 1s spectra collected with a photon energy of 600 eV at UHV and RT are displayed for all samples. A gradient fill color is applied to qualitatively highlight the trend in the ratio of pyridine-like species to hydrogenated-nitrogen species from sample to sample.

To complement the XPS analysis of the N 1s core level, surface-sensitive analysis of the Fe oxidation state distribution in each sample was performed by collecting the Fe $L_{3,2}$-edge using soft X-rays and in TEY mode. Such measurements have an information depth on the order of several nanometers or less.[41,55] Capabilities at end-station 11.0.2 at the ALS user facility enables sXAS measurements to be performed sequentially with XPS measurements, and so the sXA spectra displayed in Figure 4 were collected on the identical area of analysis and at identical environmental conditions (in the case of Figures 3 and 4, RT and UHV). Both surface sensitivity and the ability to collect XPS and sXAS at identical locations and environmental conditions distinguish this approach from more commonly seen XAS experiments in which hard X-ray sources are used.

There is a clear distinction in the features of the Fe L_3-edge dependent upon the oxidation state of the iron atoms in a sample, and approximate positions reported in the literature for pure (in terms of oxidation state) Fe(III), Fe(II), and Fe(0) compounds are indicated as dashed vertical lines in Figure 4.[42,55,57,72] First, the spectra in Figure 4 reveal that none of the samples analyzed in this work show a well-resolved peak for Fe^0. The presence of some signal at this value is due to the broad contributions from Fe(II) species because "pure" (pure in the sense of oxidation state, not necessarily pure in terms of compound or phase) Fe(II) references within the literature show a similar tail-like feature between 704 and 707 eV as well.[42,55,57,72] In all samples, two features (in the form of a peak or shoulder) at distinct values are visible at higher energies, that correspond well to the referenced positions for Fe(II) at 707.6 eV and Fe(III) at ∼709.1 eV. It is worth noting that even reference Fe(II) and Fe(III) spectra also have features (peak or shoulder) present at the position of the other oxidation state.[42,55,57,72] This result is expected because of the surface sensitivity of the sXAS measurements, as it implies that even in the case of NS-2 where STEM−EDS reveals the presence of iron particles the sampling depth is low enough such that only the outer oxide layer of the particle is detected. Among FeN_xC_y species, the distribution of oxidation states is likely related to

https://dx.doi.org/10.1021/acs.jpcc.0c05244
J. Phys. Chem. C 2020, 124, 16529−16543

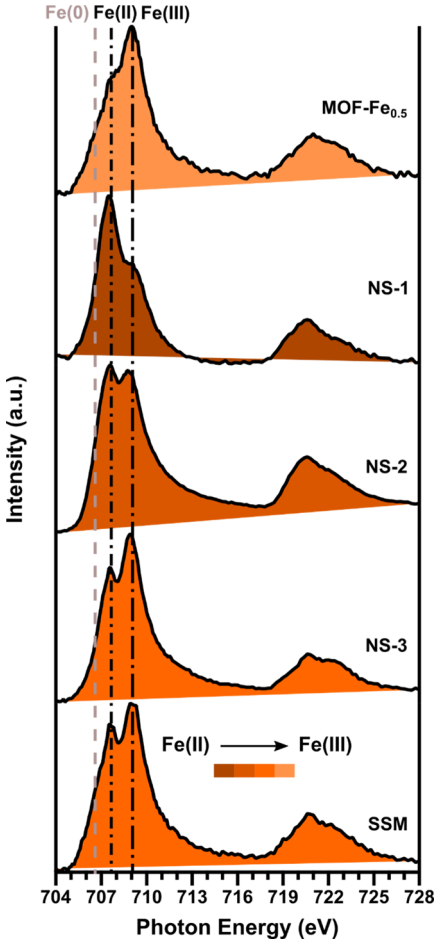

Figure 4. XAS Fe $L_{3,2}$-edge spectra collected at UHV and RT are displayed. Dashed vertical lines were added to indicate literature positions obtained on reference Fe(0), Fe(II), and Fe(III) species. A gradient fill color was also added to qualitatively reveal the trend in average Fe oxidation state of the samples.

the relative proportion of sites that contain adsorbed O_2 and are in an Fe(III) state versus those that do not and are in an Fe(II) state. Based on the Fe $L_{3,2}$-edge data, the MOF-$Fe_{0.5}$ sample has the greatest relative contribution from Fe(III) within the sample set, and its Fe $L_{3,2}$-edge spectrum is in fact close to that of pure ferric compounds in the literature.[57,72] The NS-3 and SSM samples have sXA spectra most similar to those of MOF-$Fe_{0.5}$; however, they do have a greater relative contribution from the peak at ~707.6 eV, definitively indicating the presence of Fe(II) species. NS-2 has peaks of near equal intensity at the positions corresponding to Fe(II) and Fe(III) states. Finally, the NS-1 sample has a much more intense Fe(II) peak than Fe(III) and is the closest within the dataset to a purely Fe(II) species. The varying distribution of surface Fe oxidation states revealed by the UHV sXAS results suggest that multiple Fe moieties are present within the dataset, despite all samples excluding NS-2 containing only highly dispersed Fe species, as shown in Figures 1 and 2. As both oxide species and FeN_xC_y moieties may exist in either Fe(II) or Fe(III) states, further characterization is needed to identify these Fe moieties.

3.2. Ex Situ, Ambient-Air Characterization: ^{57}Fe Mössbauer Spectroscopy. The chemical and electronic state of Fe within the catalysts was investigated through ^{57}Fe Mössbauer spectroscopy. It is important to note that in contrast to the sXAS results shown in Figure 4, ^{57}Fe Mössbauer spectroscopy is a bulk technique and therefore may detect species that are inaccessible or present in different proportions than identified with more surface-sensitive measurements. Additionally, ^{57}Fe Mössbauer spectroscopy was performed without exposing the samples to vacuum, preserving the properties of a sample exposed to the ambient atmosphere. Figure 5 shows that there are significant differences in each

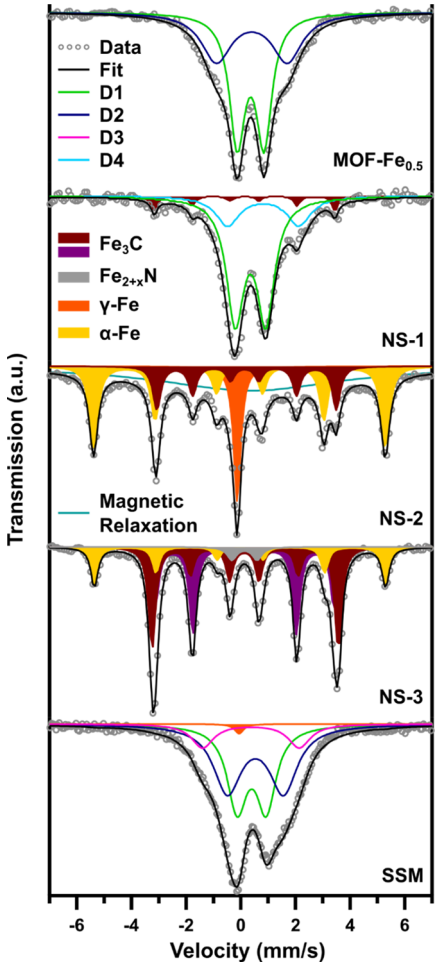

Figure 5. Experimental ^{57}Fe Mössbauer spectra collected at RT for each Fe-N-C sample and their fitting. Fitting parameters and assignment of the components to Fe species are available in Table S1. Solid lines without fill (D1−D4) represent FeN_xC_y species, while metallic, carbide, and nitride are shown with a solid fill beneath the curve.

sample's Mössbauer spectrum, which can be correlated to the presence of different Fe species through a rigorous curve fitting procedure, the results of which are displayed in Figure 5, with the fitting parameters and relative contributions of the different spectral features shown in Table S1.

The MOF-$Fe_{0.5}$ sample is the least heterogeneous, with the fitting adequate with only two spectral components, namely, the quadrupole doublets D1 and D2. As discussed previously, the exact assignment of D1 and D2 has been the subject of recent discussions within the field. Based on the previous findings, D1 is assigned to a surface $Fe(III)N_4C_{12}$ species with the presence of an adsorbed O_2 molecule, whereas D2 is assigned to $Fe(II)N_4C_{10}$ species that are likely O_2-inaccessible.[26,67] This fit suggests that the MOF-$Fe_{0.5}$ sample likely

https://dx.doi.org/10.1021/acs.jpcc.0c05244
J. Phys. Chem. C 2020, 124, 16529−16543

only contains FeN_xC_y species. NS-1 has a somewhat similar spectrum compared to that of the MOF-$Fe_{0.5}$ sample, as it also has the greatest relative contribution from the D1 component (70.7%). Although a second quadrupole doublet is also present in NS-1 (labeled D4), with a QS value similar to that of D2 (2.61 mm·s^{-1}, Table S1), this component has a significantly higher IS than D2 in the previous sample, 0.82 versus 0.40 mm·s^{-1}. Such a high IS value has been reported before for Fe(II) cations in tetrahedral coordination, whereas D2 is viewed as a near square-planar coordination.[35] D4 is therefore tentatively assigned to a distorted $Fe(II)N_xC_y$ structure—possibly present in the NS-1 sample and not MOF-$Fe_{0.5}$ because of different localized properties of the carbon matrix in NS-1 that result from its lower pyrolysis temperature. Additionally, NS-1 has a small contribution (ca. 6%) from a sextet component unambiguously assigned to Fe_3C. Therefore, it can be concluded that NS-1 is also composed of primarily FeN_xC_y species, especially the surface species hypothesized to contain an Fe(III) center because of adsorbed O_2 (D1), with a small contribution from iron carbide. Iron carbide is usually encapsulated in a N-doped carbon shell after pyrolysis, and such structures have shown some ORR activity but (on a basis per Fe mass) are much less active than FeN_xC_y sites.[73] NS-2 has a significantly different Mössbauer spectrum compared to MOF-$Fe_{0.5}$ and NS-1, with no quadrupole doublet components. The main spectral features in NS-2 are (i) a singlet component with an IS near 0 mm·s^{-1}, easily assigned to γ-Fe (Table S1), and (ii) two sextets assigned to Fe_3C and α-Fe. To complete the fit, a second and very broad singlet was necessary, reflecting an unresolved environment due to magnetic and/or electronic relaxation. The presence of metallic iron phases in NS-2 is in good agreement with the STEM−EDS results shown in Figure 2, which revealed regularly occurring iron particles. Because of the absence of FeN_xC_y-type species in NS-2, it is reasonable to conclude that NS-2 would be less ORR-active than the others in acidic medium. The fitted spectrum for NS-3 consists of three sextets assigned to α-Fe and Fe_3C and a doublet assigned to an iron nitride ($Fe_{2+x}N$) species. For a best fit, two sextets with slightly different hyperfine fields (20.3 and 21.1 T) were introduced, assigned to Fe_3C or Fe-carbide in slightly different compositions. According to the STEM−EDS (Figure 2), the Fe dispersion is very similar to NS-1, showing only highly dispersed species that must be either ultrafine particles or atomically dispersed Fe coordinated to C rather than N as in an FeN_xC_y moiety. Because NS-3, like NS-2, contains no or almost no FeN_xC_y-type species it is also expected to have low ORR activity in acidic medium. The last sample, SSM, has a spectrum more similar to the MOF-$Fe_{0.5}$ and NS-1 samples, as both D1 and D2 are present and account for the majority of the total signal. However, an additional doublet (D3) is also present, with IS similar to that of D1 and D2, but with significantly higher QS than D2, namely, 3.54 mm·s^{-1}. The QS value of this fitted D3 component is well in line with QS values recently calculated for $Fe(II)N_4C_{10}$ moieties in medium (S = 1) spin state.[26] The latter were in the range of 2.6−3.4 mm·s^{-1} for all cluster or periodic calculations of $Fe(II)N_4C_{10}$ moieties in S = 1 spin state, significantly higher than all other QS calculated for other spin states, oxidation states, or moiety structures (e.g., FeN_4C_{12}).[26] The presence of D3 in the SSM sample may be related to its higher graphitization or ordering because FeN_4C_{10} moieties are in-plane moieties embedded in an ordered graphene sheet. γ-Fe is also present in very small quantities, likely encapsulated within carbon layers because the SSM sample was subjected to acid leaching and therefore electrolyte-exposed metallic iron species are expected to have been removed from the sample. Further studies of O_2 adsorption with both nAP-XPS and sXAS are therefore necessary to evaluate the hypothesis that the more active Fe-containing MOF-$Fe_{0.5}$ and SSM species contain an adsorbed O_2 molecule on some of their FeN_xC_y surface sites and whether interactions with O_2 on FeN_xC_y-type species can be differentiated from O_2 interactions with less active NC and Fe-based species.

3.3. In Situ Characterization at 100 mTorr O_2 and 80 °C: nAP-XPS and sXAS. The first proposed step of the ORR is the adsorption of an O_2 molecule to a catalytically active site,[74] and so identifying adsorbing sites is a necessary component of understanding the ORR. Additionally, most PEMFCs are operated at elevated temperature, with 80 °C the standard value. Therefore, both XP and sXA spectra were collected on the exact same area of analysis as the UHV measurements (Figures 3 and 4) in an atmosphere of 100 mTorr of O_2 at 80 °C, such that changes in both nitrogen and iron chemistry can be observed. Within XPS N 1s spectra, previous studies have shown slight changes in the N 1s when NC and Fe−N−C samples have been exposed to O_2.[52,53] Assuming the adsorption is a relatively weak interaction between the O_2 molecule and an adsorbing atom, the electron density of the adsorbent will be disrupted and a slight shift will result in the XP spectra. To isolate these subtle changes, a difference spectrum can be calculated by subtracting the spectrum acquired in UHV from that acquired in the O_2 atmosphere. With this convention, a negative peak in the difference spectrum is indicative of an adsorbing species, as there is now less signal at the position of an adsorbent because of the shift induced by the covalent interaction with the O_2 molecule.[52] The position of this negative peak can then be correlated with a nitrogen species as in assigning components of a curve fit to specific species. An experimentally determined threshold is applied to the difference spectra to remove minor features—the threshold is set by repeating the N 1s measurement with identical conditions on a single spot to account for instrumental fluctuations. Using this method, any adsorbing sites occurring in such a low density that their change due to O_2 exposure is less than the changes in spectra due to the repeatability of the same measurement are not included.

Figure 6a shows N 1s spectra (normalized by the total peak area) acquired in UHV conditions at RT and in 100 mTorr O_2 at 80 °C, whereas Figure 6b shows the resulting difference spectra. Adsorption features in the difference spectra can be assigned to either primarily hydrogenated nitrogen (higher BE) or primarily electron-rich pyridine-like nitrogen species (lower BE), with some subtle differences present in the electron-rich adsorption peaks and peak positions. Overall, the MOF-$Fe_{0.5}$ sample, NS-2, and NS-3 all result in difference spectra indicating that adsorption occurs at both hydrogenated nitrogen and pyridine-like nitrogen to a fairly even degree, with the MOF-$Fe_{0.5}$ sample showing a slight preference for adsorption to hydrogenated species. The NS-1 and SSM samples show significant adsorption only at either low or high BE, with NS-1 having a preference for adsorption to electron-rich species and SSM for adsorption to hydrogenated nitrogen species. By relating the information provided in these difference spectra to the conclusions from ex situ characterization, it is possible to gain insight into O_2 interactions.

https://dx.doi.org/10.1021/acs.jpcc.0c05244
J. Phys. Chem. C 2020, 124, 16529−16543

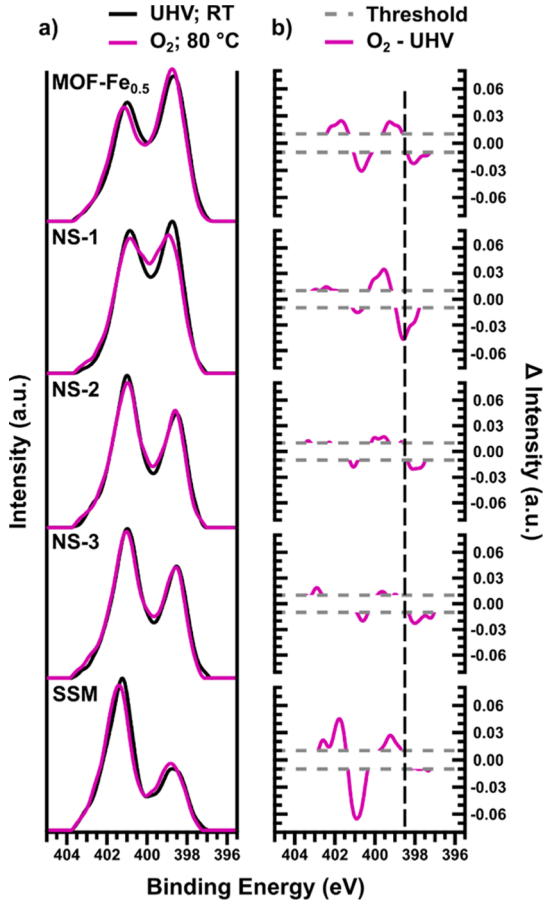

Figure 6. Overlaid, background subtracted N 1s spectra normalized to the total region area are displayed for both UHV, RT, and 100 mTorr O_2, 80 °C environments for all samples (a), alongside the resulting difference spectra (b). A dashed vertical line is included at ∼398.6 eV to draw attention to the shift in adsorption peak position unique to NS-1.

Toward this end, we first consider the case of NS-2 and NS-3, samples which do not have any FeN_xC_y species. These two samples have very similar UHV N 1s spectra and very similar difference spectra, suggesting that they have the same nitrogen sites available for O_2 adsorption. There are two negative peaks in the difference spectra of NS-2 and NS-3, present at positions most likely corresponding to hydrogenated nitrogen (∼400.6 eV) and electron-rich nitrogen (∼398 eV), species which have previously been shown to adsorb O_2 in similar Fe-free NC materials.[52] Considering the two most active samples next, both the MOF-$Fe_{0.5}$ and the SSM difference spectra only show peaks consistent with adsorption to NC species. Adsorption occurs at both classes of NC species on the MOF-$Fe_{0.5}$ sample, whereas the SSM sample has one clearly defined adsorption peak at 401.0 eV—this value is between that of hydrogenated nitrogen species and graphitic nitrogen species, and so, a clear assignment of adsorption to one class of nitrogen functionality is not possible. Interestingly so, for the MOF-$Fe_{0.5}$ and SSM catalysts, no adsorption peaks are visible within the BE range (400−398.5 eV) where the N−Fe bonds from FeN_xC_y species are typically assigned. Therefore, we can consider the desorption/adsorption events occurring on MOF-$Fe_{0.5}$ and SSM samples from UHV/100 mTorr O_2 as most likely because of N-functionalities on the surface of the N-doped carbon matrix. The results for NS-1 present a unique case. The main adsorption peak is present at 398.6 eV and is asymmetric with a shoulder at lower BE consistent with the electron-rich adsorption features present in the rest of the sample set. However, the main position of this feature is unique across the sample set as highlighted by the dashed vertical line added to Figure 6b at 398.6 eV. There are two possible assignments for this unique adsorption feature. Either NS-1 contains a different type of electron-rich NC species at the surface or adsorption is occurring at an FeN_xC_y site. A recent study has assigned an FeN_xC_y species to this BE value.[71] Additionally, in our prior study of O_2 adsorption on Fe-free NC samples, not a single Fe-free NC sample (including the Fe-free analogues to the NS samples included in this study) demonstrated an adsorption peak at this BE value.[52] Therefore, we attribute the peak at 398.6 eV to adsorption of O_2 at an FeN_xC_y moiety.

An additional set of measurements were performed in a humidified O_2 atmosphere by introducing 100 mTorr of H_2O vapor to the already present 100 mTorr of O_2. The sequential nature of this approach enables investigation of adsorption of O_2 and/or H_2O molecules to any available sites (Figure S2), as it is possible that humidification may change the adsorption properties of O_2 to different sites. Across the sample set, a slight increase in adsorption at lower BE values is observed, suggesting that water vapor adsorption to pyridinic nitrogen species, and in the case of NS-1, FeN_xC_y species, is favorable. Interestingly, the samples with the most O_2 adsorption to hydrogenated nitrogen (MOF-$Fe_{0.5}$ and SSM) show no increase in adsorption to hydrogenated nitrogen and even a very slight decrease in this feature. This suggests that water vapor adsorption to such species, in the context of a sample with adsorbed O_2 already present, is unfavorable. Further evaluation of competitive adsorption between O_2 and H_2O vapor through the introduction of premixed humidified O_2 with systematically varied relative humidity to possibly correlate adsorption with gas transport properties of different catalysts is feasible; however, this is beyond the scope of this work.

Changes in the Fe oxidation state upon exposure to O_2 were evaluated using sXAS performed in the same 100 mTorr O_2, 80 °C environment (Figure 7). Previous studies have hypothesized and provided evidence that upon O_2 adsorption, the iron atom in an FeN_x site will oxidize from Fe(II) to Fe(III).[26,32,40−42] The majority of Fe on the surface of the MOF-$Fe_{0.5}$ sample is in the Fe (III) state, and there is little to no change in the oxidation state upon exposure to O_2 for this sample. Although the MOF-$Fe_{0.5}$ sample displayed the least amount of change in the iron oxidation state across the sample set, NS-1 holds the other extrema with the greatest degree of change in the oxidation state. In UHV, NS-1 is primarily Fe(II); however, upon exposure to O_2, the surface oxidation state switches to primarily Fe(III) species. The significant change in the oxidation state of surface Fe in NS-1 corroborates the assignment of the nAP-XPS N 1s adsorption peak identified as an FeN_xC_y species. Both NS-2 and NS-3 show an increase in Fe(III) character, which must be due to species other than FeN_xC_y since no FeN_xC_y species are expected for these samples because of the absence of doublets in their Mössbauer spectra. NS-2 has a very slight increase in Fe(III) character and in O_2, is slightly more Fe(III) rich than Fe(II), and yet still has the most even distribution of oxidation states in the dataset. NS-3 experiences a slightly larger relative increase in Fe(III) signal upon exposure to O_2, resulting in an O_2 atmosphere spectrum that is primarily Fe(III). Therefore,

https://dx.doi.org/10.1021/acs.jpcc.0c05244
J. Phys. Chem. C 2020, 124, 16529−16543

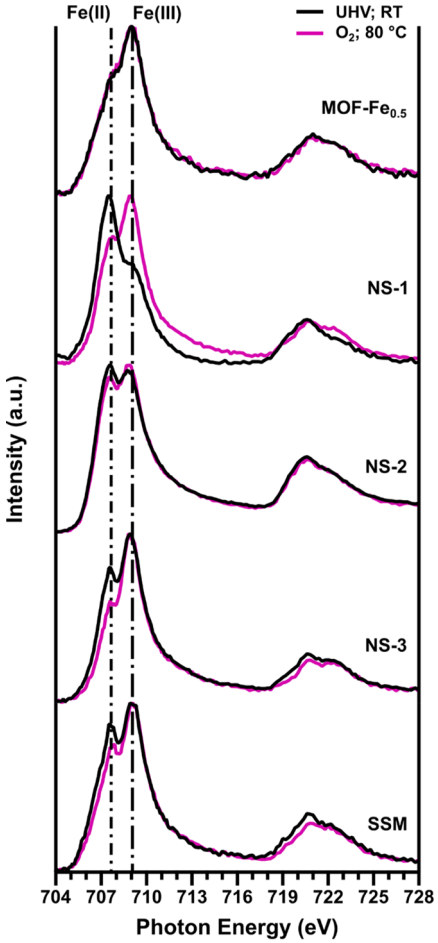

Figure 7. sXAS Fe $L_{3,2}$-edge spectra collected at UHV and RT, and 100 mTorr O_2 and 80 °C are displayed for all samples. Dashed vertical lines were added to XA spectra to indicate literature positions obtained on references for Fe(II) and Fe(III) species.

the most likely explanation for the change in the oxidation state is a partial conversion of surface oxide species present on (metallic or carbide) Fe particles, from FeO to Fe_3O_4 or Fe_2O_3, or from Fe_3O_4 to Fe_2O_3.[75] As shown in Figure 2, NS-2 has Fe particles on the order of tens of nanometers, whereas NS-3 has highly dispersed Fe either in the form of ultrafine (a few nm or less) particles or atomically dispersed complexes; it follows that NS-2 experiences less change upon exposure to O_2. Finally, there is a slight increase in the Fe(III) character for the SSM sample, representing an intermediate case to MOF-$Fe_{0.5}$ and NS-1. To explain the different responses to the introduction of O_2 observed through sXAS among the five samples, we now present a discussion of the results in the context of the results of all of the characterization techniques employed and the differences in processing history of the samples.

4. DISCUSSION

Having thoroughly characterized each material with STEM−EDS, ^{57}Fe Mössbauer spectroscopy, and XPS and sXAS (both UHV and in an O_2 atmosphere), the properties of each sample and how these properties drive the material's interactions with O_2 can be interpreted. Two of the model NS samples (NS-2 and NS-3) were not found to contain any FeN_xC_y-type species and therefore provide excellent baseline examples of how less active or inactive NC and Fe species interact with O_2. Indeed, electrochemical evaluation through RRDE shown in Figure S3 indicates little activity for these two samples. NS-2 and NS-3 had very similar size, shape, morphology, spatial distribution of nitrogen, and chemical speciation of nitrogen, and therefore, it follows that NS-2 and NS-3 had essentially the same set of interactions between nitrogen species and O_2, with adsorption present at electron-rich, pyridine-like species as well as hydrogenated nitrogen species, a result very similar to that of Fe-free NS analogues previously published.[52] The major difference between these samples was the distribution of their Fe species—NS-2 had regularly occurring Fe particles, whereas NS-3 contained highly dispersed Fe species, revealed by Mössbauer to be primarily Fe_3C. This difference resulted in a different initial distribution of surface Fe oxidation states, as NS-2 had the most balanced ratio of Fe(III)/Fe(II) within the sample set, whereas NS-3 had more Fe(III) character than Fe(II) as revealed by UHV sXAS. Upon exposure to O_2, both samples showed a similar degree of oxidation, with an increase in the ratio of Fe(III)/Fe(II). Because of the chemical states of Fe as revealed in Mössbauer spectroscopy, it is hypothesized that this change in the oxidation state was due to an enrichment of Fe(III) species within the extreme surface oxide layers of metallic, carbide, or nitride iron species present. It is not expected that the interactions between N-containing species and O_2 in these samples have any connection to the interactions between the Fe-containing species that result in the change in the Fe oxidation state. The relative increase in the Fe(III)/Fe(II) ratio upon exposure to O_2 among NS-2 and NS-3 is greater than that of both the MOF-$Fe_{0.5}$ and SSM samples, which are known to be ORR active.[10,32,61,76]

The MOF-$Fe_{0.5}$, NS-1, and SSM samples all contain FeN_xC_y species, as shown by the presence of doublets D1−D4 in their Mössbauer spectra (Figure 5). However, these materials have significantly different structures, and all have variations in the exact distribution of FeN_xC_y moieties present. To aid in the discussion and differentiation of O_2 adsorption behavior observed among these three samples, a cartoon depiction of three cases of O_2 interaction with a generalized FeN_xC_y site is displayed in Figure 8. Note that exact details of the structure, coordination, geometry, and O_2 orientation are not meant to be covered by this cartoon, rather it is used to highlight changes in the iron oxidation state that can be detected spectroscopically in different environments because of either the presence or absence of adsorbed O_2. Case 1 represents a strong interaction between O_2 and the FeN_xC_y species. This results in the adsorption of O_2 from ambient air, and the presence of an Fe(III) center during characterization at such conditions (^{57}Fe Mössbauer spectroscopy, Figure 5). Upon exposure to UHV environments (XPS and sXAS in Figures 3 and 4), the strongly adsorbed O_2 molecules are still present, and therefore, the Fe(III) state is preserved. In this case, no changes in adsorption behavior or iron oxidation state from UHV to the O_2-rich atmosphere (nAP-XPS and sXAS, Figures 6 and 7) will be observed. For Case 1, the Fe center remains as Fe(III) because of the persistence of adsorbed O_2 throughout all experimental conditions investigated in this work. Case 2 represents a weaker interaction between O_2 and FeN_xC_y sites. In Case 2, O_2 is still adsorbed at ambient conditions, resulting in an Fe(III) center as in Case 1. The major distinction occurs upon exposure to UHV—this hypothesized weaker interaction results in desorption of O_2 and detection of an Fe(II) center during measurements taking place under UHV conditions.

https://dx.doi.org/10.1021/acs.jpcc.0c05244
J. Phys. Chem. C 2020, 124, 16529−16543

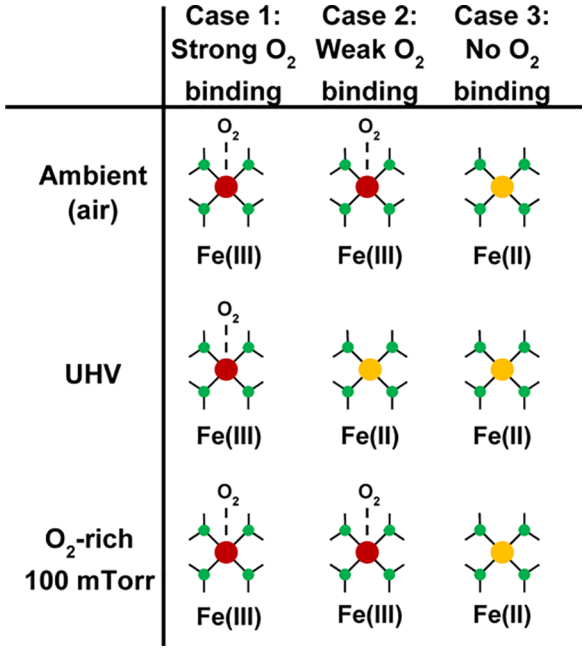

Figure 8. Scheme of different O_2 adsorption behavior on FeN_xC_y sites for each of the relevant atmospheres corresponding to different characterization atmospheres. Green circles are used to represent nitrogen atoms, while Fe(III) cations are represented by red circles and Fe(II) cations by yellow circles.

Upon re-exposure to O_2, this FeN_xC_y site readsorbs O_2, and therefore, an Fe(III) center is detected. It is likely that Fe-free NC sites such as pyridine or hydrogenated nitrogen follow this case as well, as they are identifiable in nAP-XPS measurements (Figure 6). Finally, Case 3 represents FeN_xC_y sites that do not interact with O_2 in any atmosphere, and therefore are always in an Fe(II) state. Case 3 is representative of inaccessible FeN_xC_y species, and/or FeN_xC_y species in which O_2 interaction is unfavorable, whereas Case 1 and Case 2 are representative of surface FeN_xC_y species with different O_2 binding behavior. The latter is most likely tuned by differences in the properties of their surrounding carbonaceous matrix or the exact structure/coordination of the site.

We first discuss MOF-$Fe_{0.5}$, as it only contains two doublet features in its Mössbauer spectrum, both assigned to the FeN_xC_y family of species. FeN_xC_y species assigned to D1 are considered to be O_2-accessible at the surface and in an Fe(III) state due to adsorbed O_2, whereas D2 is inaccessible and therefore has no adsorbed O_2, and is in an Fe(II) state. Therefore, we can conclude that D2 most likely follows Case 3 and does not interact with O_2. UHV sXAS of MOF-$Fe_{0.5}$ shows the highest Fe(III)/Fe(II) ratio of all samples, and there is little to no change in the Fe(III)/Fe(II) ratio from sXAS upon re-exposure to O_2. This result suggests that O_2 molecules are bound to the $Fe(III)N_xC_y$ structures of D1 in all environments investigated, preventing any detectable change in the oxidation state of Fe when O_2 is introduced, as described in Case 1. The strong binding of O_2 on all the Fe-based surface sites in MOF-$Fe_{0.5}$ is in line with a recent CO chemisorption study on an exact analogue of the same sample, showing that a fraction of FeN_x surface sites could be freed from preadsorbed O_2 only after a cleaning treatment at a temperature of at least 300 °C, but a cleaning temperature of 600 °C was necessary to remove most or all preadsorbed O_2.[67] nAP-XPS results also indicate no adsorption peak at a BE value that could be assigned to an adsorption on FeN_xC_y species, corroborating the in situ sXAS results. Therefore, we conclude that the MOF-$Fe_{0.5}$ sample contains only FeN_xC_y species that fall into Case 1 or Case 3, where those represented by D1 in Figure 5 are surface sites with strongly bound O_2 that most likely contribute to catalytic activity, and those represented by D2 are not O_2-accessible and therefore are unlikely to contribute to ORR activity.

We consider SSM next, which has slightly different O_2 interaction behavior relative to the MOF-$Fe_{0.5}$ sample. Within the Mössbauer spectrum for SSM, three doublets are present that correspond to FeN_xC_y species. D1 and D2 are present within MOF-$Fe_{0.5}$ as well, whereas D3 is unique to this sample. D2 and D3 are assigned to similar species because both are $Fe(II)N_xC_y$ and are likely inaccessible as they do not show interactions with O_2 from the air. This hypothesis suggests that any changes in Fe(III)/Fe(II) ratio detected in sXAS experiments must be due to either FeN_xC_y species contributing to the D1 signal or another Fe-based species like in NS-2 or NS-3. Indeed, there is a slight increase in Fe(III)/Fe(II) in the O_2-rich environment when compared to the UHV environment detected by sXAS (Figure 7). Although the SSM sample's Mössbauer spectrum does show a small contribution from γ-Fe, it is only 1.1% of the total signal and therefore unlikely to account for the change in the oxidation state. Furthermore, the SSM sample was acid treated to remove particulate iron, and therefore, the remaining γ-Fe must be coated by a carbon shell, rendering it also unlikely to be O_2-accessible or even detectable by surface-sensitive sXAS measurements. Therefore, we hypothesize that SSM contains a distribution of FeN_xC_y sites that are identical within its Mössbauer spectrum and contribute to D1 and yet have different strengths of O_2 adsorption. The majority of D1 FeN_xC_y sites likely follow Case 1 as in MOF-$Fe_{0.5}$, but a small amount must follow Case 2 to explain the slight increase in Fe(III) character in O_2-rich sXAS measurements. This difference in adsorption strength is hypothesized to be due to slight differences in the carbon matrix surrounding the FeN_xC_y site, for example, in-plane versus edge location and degree of graphitization versus defected nature of the carbon plane.[18] As Mössbauer spectroscopy will not easily identify differences beyond the first coordination shell of iron, it is conceivable that identical spectral components within a Mössbauer spectrum are not located in the same environment and therefore have different O_2 adsorption strengths, influenced by the properties of the carbon structure. Indeed, the presence of both D2 and D3 within SSM, which are similar $Fe(II)N_4C_{10}$ species with D3 hypothesized to be embedded in a highly ordered graphitic carbon plane, while D2 may be present in a less ordered carbon plane, implies that D1 may contain (spectroscopically identical) sites in different carbon environments. As the SSM sample contains both micro- and meso-pores (while mostly micropores are present in MOF-$Fe_{0.5}$), it is possible that FeN_xC_y sites hosted within different pore structures explains the hypothesized difference in O_2 binding strength and the observed change in iron oxidation state upon exposure to the O_2-rich environment.

Finally, we consider NS-1 which has two doublets in its Mössbauer spectrum, D1 and D4. Although D1 must fall into Case 1 or Case 2 because of its assignment to $Fe(III)N_xC_y$ with adsorbed O_2 present, D4 is assigned to an $Fe(II)N_xC_y$ species in a tetrahedral configuration. This assignment containing an Fe(II) center suggests that D4, like D2 and

https://dx.doi.org/10.1021/acs.jpcc.0c05244
J. Phys. Chem. C 2020, 124, 16529−16543

D3, is likely O_2 inaccessible and can be assumed to belong to Case 3. Under UHV conditions, NS-1 has the lowest Fe(III)/Fe(II) ratio (Figure 4) of all samples. This suggests that the adsorbed O_2 (present on D1 sites in the Mössbauer spectrum acquired in air, Figure 5) has desorbed in UHV conditions. Upon re-exposure to O_2 the Fe(III)/Fe(II) ratio drastically switches to Fe(III) rich (Figure 7), and an adsorption peak assignable to FeN_xC_y species is present in the nAP-XPS difference spectrum (Figure 6). This suggests that surface FeN_xC_y sites in NS-1 follow primarily Case 2 and interact with O_2 more weakly than those of MOF-$Fe_{0.5}$ and also more weakly than the majority of surface FeN_xC_y sites in the SSM sample. Although, because of its synthesis, most of the sites present in the model NS-1 sample should be accessible for catalyzing the ORR, it is expected that they have a lower ORR activity than those in MOF-$Fe_{0.5}$ and SSM. The ORR activity of NS-1 was screened by RRDE in Figure S3, with a resulting half-wave potential estimated between ∼0.57 and ∼0.64 V versus RHE, depending on the catalyst loading used. This value is ∼0.2−0.25 V lower than the more active SSM and MOF-$Fe_{0.5}$ catalysts.[10,33,62] From this analysis, we cannot definitively conclude whether some FeN_xC_y sites in NS-1 interact strongly with O_2 and follow Case 1 or not; however, the strikingly larger magnitude of change in iron oxidation state observed for NS-1 relative to the rest of the dataset certainly suggests that the majority of FeN_xC_y sites interact weakly with O_2, and is supported by the lower activity of this sample.

Each of the three samples containing FeN_xC_y sites shows different O_2 adsorption behavior; however, this is more likely to be due to differences in the local carbon structure than due to detectable differences in the FeN_xC_y species. Only species that contribute to the D1 feature (observed in the Mössbauer spectrum measured in air) are present in an Fe(III) state in air (i.e., with O_2 adsorbed), and therefore, the other three FeN_x species identified (D2−D4) are either O_2-inaccessible or unfavorable for O_2 adsorption. Therefore, we attribute differences in O_2 adsorption strengths among the different samples to similar D1 sites but that are embedded in different local environments. This result has two major implications, the first of which highlights the ambiguity and potential pitfalls of treating all FeN_xC_y species contributing to a given spectroscopic feature in a Mössbauer spectrum acquired in ambient conditions as identical. In this work, we discuss the D1 feature in Mössbauer spectrum often attributed to catalytic activity in detail; however, this principle can be extended to other characterizations (such as XAS and XPS where detailed curve-fitting is often employed to identify FeN_xC_y species) within this work as well. Depending on the nature of the work, it can be very important to consider the exact spectroscopic information that an assignment of a component to a physical species is based upon and whether other properties outside of those measured may influence the catalytic properties of a given species. Multi-technique studies that investigate different relevant environments are also necessary to understand such complex chemical species and systems. The second major implication is that the nature of the carbon matrix an active site is hosted in can influence its O_2 interaction strength and therefore likely its specific activity (turnover frequency) as well. Of the three samples with FeN_xC_y sites, NS-1 experienced a much lower pyrolysis temperature (600 °C) than MOF-$Fe_{0.5}$ and SSM (≥1000 °C), and NS-1 is less active than the MOF-$Fe_{0.5}$ and SSM samples. This should result in more ordered, graphitic carbon in the MOF-$Fe_{0.5}$ and SSM samples than in NS-1. Considering the weak O_2 interaction characteristic of the model NS-1 sample, it suggests that increased graphitization of the carbon matrix may be responsible for stronger interactions with O_2, among other beneficial changes in conductivity and stability in acidic medium, ultimately resulting in higher ORR activity.[18,68] This result highlights the importance of further characterization studies to continue to gain further clarity and improve the reliability in identifying different strengths of O_2 interaction with FeN_xC_y moieties and to better understand their specific structures and properties for correlation with ORR activity and fuel cell performance.

5. CONCLUSIONS

In this study, five Fe−N−C samples are thoroughly characterized, both ex situ under UHV (STEM−EDS, XPS, and sXAS), ex situ under ambient conditions (^{57}Fe Mössbauer spectroscopy), and in situ in the presence of O_2 at 80 °C (nAP-XPS and sXAS). Based on comprehensive characterization results, this work provides further evidence of the presence of adsorbed O_2 species on certain FeN_xC_y species, while also suggesting that other FeN_xC_y species may not interact with O_2 as strongly or at all. We provide evidence in support of the hypothesis that the FeN_xC_y site present in the most active samples, MOF-$Fe_{0.5}$ and SSM, and assigned to D1 in Mössbauer spectra, strongly adsorbs O_2 from air such that they exist in an Fe(III) state. The model sample which also primarily contains iron in FeN_xC_y-type sites, NS-1, contains FeN_xC_y sites that do not interact as strongly with O_2 as those in the MOF-$Fe_{0.5}$ and SSM samples. This is most likely due to a difference in the localized carbon matrix surrounding the FeN_xC_y sites produced at a significantly lower heat treatment temperature—600 °C for NS-1 versus ≥1000 °C for MOF-$Fe_{0.5}$ and SSM. This study has significant implications on further synthesis efforts and spectroscopic characterization studies toward the goal of identifying, differentiating, and producing exact species within the FeN_xC_y family of structures. This will enable further evaluation of their relative activity, both for ORR and for other relevant catalytic reactions, and highlights the necessity of conducting multitechnique characterization studies encompassing measurements in varied environments.

■ ASSOCIATED CONTENT

Supporting Information

The Supporting Information is available free of charge at https://pubs.acs.org/doi/10.1021/acs.jpcc.0c05244.

C 1s nAP-XPS data and accompanying discussion; ^{57}Fe Mössbauer spectroscopy fitting parameters; results of nAP-XPS measurements in a humidified O_2 atmosphere; RRDE measurements of samples NS-1, NS-2, and NS-3; and associated discussion and experimental details (PDF)

■ AUTHOR INFORMATION

Corresponding Author

Svitlana Pylypenko − *Department of Chemistry, Colorado School of Mines, Golden, Colorado 80401, United States;* orcid.org/0000-0001-7982-734X; Phone: (303) 384-2140; Email: spylypen@mines.edu

https://dx.doi.org/10.1021/acs.jpcc.0c05244
J. Phys. Chem. C 2020, 124, 16529−16543

Authors

Michael J. Dzara − *Department of Chemistry, Colorado School of Mines, Golden, Colorado 80401, United States;* orcid.org/0000-0001-8125-0586

Kateryna Artyushkova − *Physical Electronics Inc., East Chanhassen, Minnesota 55317, United States;* orcid.org/0000-0002-2611-0422

Moulay Tahar Sougrati − *ICGM, Universite de Montpellier, CNRS, ENSCM, Montpellier 34095, France;* orcid.org/0000-0003-3740-2807

Chilan Ngo − *Department of Chemistry, Colorado School of Mines, Golden, Colorado 80401, United States;* orcid.org/0000-0003-4084-098X

Margaret A. Fitzgerald − *Department of Chemistry, Colorado School of Mines, Golden, Colorado 80401, United States;* orcid.org/0000-0003-2976-0145

Alexey Serov − *Pajarito Powder, LLC, Albuquerque, New Mexico 87102, United States*

Barr Zulevi − *Pajarito Powder, LLC, Albuquerque, New Mexico 87102, United States*

Plamen Atanassov − *Department of Chemical & Bimolecular Engineering, National Fuel Cell Research Center (NFCRC), University of California, Irvine, California 92697, United States;* orcid.org/0000-0003-2996-472X

Frédéric Jaouen − *ICGM, Universite de Montpellier, CNRS, ENSCM, Montpellier 34095, France;* orcid.org/0000-0001-9836-3261

Complete contact information is available at: https://pubs.acs.org/10.1021/acs.jpcc.0c05244

Notes

The authors declare no competing financial interest.

■ ACKNOWLEDGMENTS

This work was supported by start-up funds from Colorado School of Mines and NSF award #1800585—Probing Catalyst-support Interactions via Experiment and Theory. This research used resources of the ALS, which is a DOE Office of Science User Facility under contract no. DE-AC02-05CH11231. We gratefully acknowledge Dr. Hendrik Bluhm for his assistance in collecting data at beamline 11.0.2 of the ALS. K.A. acknowledges NSF award # 1738386 RII Track-4: Operando Analysis of Fuel Cell Materials at ALS. A.S. and B.Z. gratefully acknowledge financial support from US DOE EERE (DE-EE0008419 "Active and Durable PGM-free Cathodic Electrocatalysts for Fuel Cell Application").

■ REFERENCES

(1) Sui, S.; Wang, X.; Zhou, X.; Su, Y.; Riffat, S.; Liu, C.-j. A Comprehensive Review of Pt Electrocatalysts for the Oxygen Reduction Reaction: Nanostructure, Activity, Mechanism and Carbon Support in PEM Fuel Cells. *J. Mater. Chem. A* **2017**, *5*, 1808−1825.

(2) Chen, Z.; Higgins, D.; Yu, A.; Zhang, L.; Zhang, J. A Review on Non-Precious Metal Electrocatalysts for PEM Fuel Cells. *Energy Environ. Sci.* **2011**, *4*, 3167−3192.

(3) Zhang, B.-W.; Yang, H. L.; Wang, Y. X.; Dou, S. X.; Liu, H. K. A Comprehensive Review on Controlling Surface Composition of Pt-Based Bimetallic Electrocatalysts. *Adv. Energy Mater.* **2018**, *8*, 1703597.

(4) Garlyyev, B.; Kratzl, K.; Rück, M.; Michalička, J.; Fichtner, J.; Macak, J. M.; Kratky, T.; Günther, S.; Cokoja, M.; Bandarenka, A. S.; et al. Optimizing the Size of Platinum Nanoparticles for Enhanced Mass Activity in the Electrochemical Oxygen Reduction Reaction. *Angew. Chem., Int. Ed.* **2019**, *58*, 9596−9600.

(5) Bing, Y.; Liu, H.; Zhang, L.; Ghosh, D.; Zhang, J. Nanostructured Pt-Alloy Electrocatalysts for PEM Fuel Cell Oxygen Reduction Reaction. *Chem. Soc. Rev.* **2010**, *39*, 2184−2202.

(6) Alia, S. M.; Ngo, C.; Shulda, S.; Ha, M.-A.; Dameron, A. A.; Weker, J. N.; Neyerlin, K. C.; Kocha, S. S.; Pylypenko, S.; Pivovar, B. S. Exceptional Oxygen Reduction Reaction Activity and Durability of Platinum-Nickel Nanowires through Synthesis and Post-Treatment Optimization. *ACS Omega* **2017**, *2*, 1408−1418.

(7) Strasser, P.; Kühl, S. Dealloyed Pt-Based Core-Shell Oxygen Reduction Electrocatalysts. *Nano Energy* **2016**, *29*, 166−177.

(8) Martinez, U.; Komini Babu, S.; Holby, E. F.; Chung, H. T.; Yin, X.; Zelenay, P. Progress in the Development of Fe-Based PGM-Free Electrocatalysts for the Oxygen Reduction Reaction. *Adv. Mater.* **2019**, *31*, 1970224.

(9) Zhang, H.; Chung, H. T.; Cullen, D. A.; Wagner, S.; Kramm, U. I.; More, K. L.; Zelenay, P.; Wu, G. High-Performance Fuel Cell Cathodes Exclusively Containing Atomically Dispersed Iron Active Sites. *Energy Environ. Sci.* **2019**, *12*, 2548−2558.

(10) Serov, A.; Artyushkova, K.; Niangar, E.; Wang, C.; Dale, N.; Jaouen, F.; Sougrati, M.-T.; Jia, Q.; Mukerjee, S.; Atanassov, P. Nano-Structured Non-Platinum Catalysts for Automotive Fuel Cell Application. *Nano Energy* **2015**, *16*, 293−300.

(11) Armel, V.; Hindocha, S.; Salles, F.; Bennett, S.; Jones, D.; Jaouen, F. Structural Descriptors of Zeolitic-Imidazolate Frameworks Are Keys to the Activity of Fe-N-C Catalysts. *J. Am. Chem. Soc.* **2017**, *139*, 453−464.

(12) Wood, K. N.; O'Hayre, R.; Pylypenko, S. Recent Progress on Nitrogen/Carbon Structures Designed for Use in Energy and Sustainability Applications. *Energy Environ. Sci.* **2014**, *7*, 1212.

(13) Workman, M. J.; Dzara, M.; Ngo, C.; Pylypenko, S.; Serov, A.; McKinney, S.; Gordon, J.; Atanassov, P.; Artyushkova, K. Platinum Group Metal-Free Electrocatalysts: Effects of Synthesis on Structure and Performance in Proton-Exchange Membrane Fuel Cell Cathodes. *J. Power Sources* **2017**, *348*, 30−39.

(14) Ferrero, G. A.; Preuss, K.; Marinovic, A.; Jorge, A. B.; Mansor, N.; Brett, D. J. L.; Fuertes, A. B.; Sevilla, M.; Titirici, M.-M. Fe-N-Doped Carbon Capsules with Outstanding Electrochemical Performance and Stability for the Oxygen Reduction Reaction in Both Acid and Alkaline Conditions. *ACS Nano* **2016**, *10*, 5922−5932.

(15) Ratso, S.; Ranjbar Sahraie, N.; Sougrati, M. T.; Käärik, M.; Kook, M.; Saar, R.; Paiste, P.; Jia, Q.; Leis, J.; Mukerjee, S.; et al. Synthesis of Highly-Active Fe-N-C Catalysts for PEMFC with Carbide-Derived Carbons. *J. Mater. Chem. A* **2018**, *6*, 14663−14674.

(16) Wu, G.; Santandreu, A.; Kellogg, W.; Gupta, S.; Ogoke, O.; Zhang, H.; Wang, H.-L.; Dai, L. Carbon Nanocomposite Catalysts for Oxygen Reduction and Evolution Reactions: From Nitrogen Doping to Transition-Metal Addition. *Nano Energy* **2016**, *29*, 83−110.

(17) Artyushkova, K.; Rojas-Carbonell, S.; Santoro, C.; Weiler, E.; Serov, A.; Awais, R.; Gokhale, R. R.; Atanassov, P. Correlations between Synthesis and Performance of Fe-Based PGM-Free Catalysts in Acidic and Alkaline Media: Evolution of Surface Chemistry and Morphology. *ACS Appl. Energy Mater.* **2019**, *2*, 5406−5418.

(18) Asset, T.; Atanassov, P. Iron-Nitrogen-Carbon Catalysts for Proton Exchange Membrane Fuel Cells. *Joule* **2020**, *4*, 33−44.

(19) Artyushkova, K.; Serov, A.; Rojas-Carbonell, S.; Atanassov, P. Chemistry of Multitudinous Active Sites for Oxygen Reduction Reaction in Transition Metal-Nitrogen-Carbon Electrocatalysts. *J. Phys. Chem. C* **2015**, *119*, 25917−25928.

(20) Li, J.; Jia, Q.; Mukerjee, S.; Sougrati, M.-T.; Drazic, G.; Zitolo, A.; Jaouen, F. The Challenge of Achieving a High Density of Fe-Based Active Sites in a Highly Graphitic Carbon Matrix. *Catalysts* **2019**, *9*, 144.

(21) Choi, C. H.; Lim, H.-K.; Chung, M. W.; Chon, G.; Ranjbar Sahraie, N.; Altin, A.; Sougrati, M.-T.; Stievano, L.; Oh, H. S.; Park, E. S.; et al. The Achilles' Heel of Iron-Based Catalysts during Oxygen Reduction in an Acidic Medium. *Energy Environ. Sci.* **2018**, *11*, 3176−3182.

(22) Ferrandon, M.; Kropf, A. J.; Myers, D. J.; Artyushkova, K.; Kramm, U.; Bogdanoff, P.; Wu, G.; Johnston, C. M.; Zelenay, P.

Multitechnique Characterization of a Polyaniline − Iron − Carbon Oxygen Reduction Catalyst. *J. Phys. Chem. C* **2012**, *116*, 16001−16013.
(23) Ngo, C.; Dzara, M. J.; Shulda, S.; Pylypenko, S. Spectroscopy and Microscopy for Characterization of Fuel Cell Catalysts. *Electrocatalysts for Low Temperature Fuel Cells*; John Wiley & Sons, Ltd, 2017; pp 443−466.
(24) Wu, G. Current Challenge and Perspective of PGM-Free Cathode Catalysts for PEM Fuel Cells. *Front. Energy* **2017**, *11*, 286−298.
(25) Jia, Q.; Liu, E.; Jiao, L.; Pann, S.; Mukerjee, S. X-Ray Absorption Spectroscopy Characterizations on PGM-Free Electrocatalysts: Justification, Advantages, and Limitations. *Adv. Mater.* **2019**, *31*, 1805157.
(26) Mineva, T.; Matanovic, I.; Atanassov, P.; Sougrati, M.-T.; Stievano, L.; Clémancey, M.; Kochem, A.; Latour, J.-M.; Jaouen, F. Understanding Active Sites in Pyrolyzed Fe−N−C Catalysts for Fuel Cell Cathodes by Bridging Density Functional Theory Calculations and 57Fe Mössbauer Spectroscopy. *ACS Catal.* **2019**, *9*, 9359−9371.
(27) Matanovic, I.; Artyushkova, K.; Strand, M. B.; Dzara, M. J.; Pylypenko, S.; Atanassov, P. Core Level Shifts of Hydrogenated Pyridinic and Pyrrolic Nitrogen in the Nitrogen-Containing Graphene-Based Electrocatalysts: In-Plane vs Edge Defects. *J. Phys. Chem. C* **2016**, *120*, 29225−29232.
(28) Kabir, S.; Artyushkova, K.; Kiefer, B.; Atanassov, P. Computational and Experimental Evidence for a New TM-N_3/C Moiety Family in Non-PGM Electrocatalysts. *Phys. Chem. Chem. Phys.* **2015**, *17*, 17785−17789.
(29) Jia, Q.; Ramaswamy, N.; Hafiz, H.; Tylus, U.; Strickland, K.; Wu, G.; Barbiellini, B.; Bansil, A.; Holby, E. F.; Zelenay, P.; et al. Experimental Observation of Redox-Induced Fe-N Switching Behavior as a Determinant Role for Oxygen Reduction Activity. *ACS Nano* **2015**, *9*, 12496−12505.
(30) Matanovic, I.; Artyushkova, K.; Atanassov, P. Understanding PGM-Free Catalysts by Linking Density Functional Theory Calculations and Structural Analysis: Perspectives and Challenges. *Curr. Opin. Electrochem.* **2018**, *9*, 137−144.
(31) Kramm, U. I.; Ni, L.; Wagner, S. ^{57}Fe Mössbauer Spectroscopy Characterization of Electrocatalysts. *Adv. Mater.* **2019**, *31*, 1805623.
(32) Zitolo, A.; Goellner, V.; Armel, V.; Sougrati, M.-T.; Mineva, T.; Stievano, L.; Fonda, E.; Jaouen, F. Identification of Catalytic Sites for Oxygen Reduction in Iron- and Nitrogen-Doped Graphene Materials. *Nat. Mater.* **2015**, *14*, 937−942.
(33) Kramm, U. I.; Lefèvre, M.; Larouche, N.; Schmeisser, D.; Dodelet, J.-P. Correlations between Mass Activity and Physicochemical Properties of Fe/N/C Catalysts for the ORR in PEM Fuel Cell via ^{57}Fe Mössbauer Spectroscopy and Other Techniques. *J. Am. Chem. Soc.* **2014**, *136*, 978−985.
(34) Koslowski, U. I.; Abs-Wurmbach, I.; Fiechter, S.; Bogdanoff, P. Nature of the Catalytic Centers of Porphyrin-Based Electrocatalysts for the ORR: A Correlation of Kinetic Current Density with the Site Density of Fe-N4 Centers. *J. Phys. Chem. C* **2008**, *112*, 15356−15366.
(35) Sougrati, M. T.; Goellner, V.; Schuppert, A. K.; Stievano, L.; Jaouen, F. Probing Active Sites in Iron-Based Catalysts for Oxygen Electro-Reduction: A Temperature-Dependent ^{57}Fe Mössbauer Spectroscopy Study. *Catal. Today* **2016**, *262*, 110−120.
(36) Kramm, U. I.; Herranz, J.; Larouche, N.; Arruda, T. M.; Lefèvre, M.; Jaouen, F.; Bogdanoff, P.; Fiechter, S.; Abs-Wurmbach, I.; Mukerjee, S.; et al. Structure of the Catalytic Sites in Fe/N/C-Catalysts for O_2-Reduction in PEM Fuel Cells. *Phys. Chem. Chem. Phys.* **2012**, *14*, 11673−11688.
(37) Bouwkamp-Wijnoltz, A. L.; Visscher, W.; Van Veen, J. A. R.; Boellaard, E.; van der Kraan, A. M.; Tang, S. C. On Active-Site Heterogeneity in Pyrolyzed Carbon-Supported Iron Porphyrin Catalysts for the Electrochemical Reduction of Oxygen: An in Situ Mössbauer Study. *J. Phys. Chem. B* **2002**, *106*, 12993−13001.
(38) Schulenburg, H.; Stankov, S.; Schünemann, V.; Radnik, J.; Dorbandt, I.; Fiechter, S.; Bogdanoff, P.; Tributsch, H. Catalysts for the Oxygen Reduction from Heat-Treated Iron(III) Tetramethoxyphenylporphyrin Chloride: Structure and Stability of Active Sites. *J. Phys. Chem. B* **2003**, *107*, 9034−9041.
(39) Wagner, S.; Auerbach, H.; Tait, C. E.; Martinaiou, I.; Kumar, S. C. N.; Kübel, C.; Sergeev, I.; Wille, H. C.; Behrends, J.; Wolny, J. A.; et al. Elucidating the Structural Composition of an Fe−N−C Catalyst by Nuclear- and Electron-Resonance Techniques. *Angew. Chem., Int. Ed.* **2019**, *58*, 10486−10492.
(40) Li, J.; Ghoshal, S.; Liang, W.; Sougrati, M.-T.; Jaouen, F.; Halevi, B.; Mckinney, S.; McCool, G.; Ma, C.; Yuan, X.; et al. Structural and Mechanistic Basis for the High Activity of Fe−N−C Catalysts toward Oxygen Reduction. *Energy Environ. Sci.* **2016**, *9*, 2418−2432.
(41) Zhou, J.; Duchesne, P. N.; Hu, Y.; Wang, J.; Zhang, P.; Li, Y.; Regier, T.; Dai, H. Fe-N Bonding in a Carbon Nanotube-Graphene Complex for Oxygen Reduction: An XAS Study. *Phys. Chem. Chem. Phys.* **2014**, *16*, 15787−15791.
(42) Miedema, P. S.; van Schooneveld, M. M.; Bogerd, R.; Rocha, T. C. R.; Hävecker, M.; Knop-Gericke, A.; de Groot, F. M. F. Oxygen Binding to Cobalt and Iron Phthalocyanines as Determined from in Situ X-Ray Absorption Spectroscopy. *J. Phys. Chem. C* **2011**, *115*, 25422−25428.
(43) Zagal, J. H.; Koper, M. T. M. Reactivity Descriptors for the Activity of Molecular MN_4 Catalysts for the Oxygen Reduction Reaction. *Angew. Chem. Int. Ed.* **2016**, *55*, 14510.
(44) Tylus, U.; Jia, Q.; Strickland, K.; Ramaswamy, N.; Serov, A.; Atanassov, P.; Mukerjee, S. Elucidating Oxygen Reduction Active Sites in Pyrolyzed Metal-Nitrogen Coordinated Non-Precious-Metal Electrocatalyst Systems. *J. Phys. Chem. C* **2014**, *118*, 8999−9008.
(45) Bluhm, H.; Hävecker, M.; Knop-Gericke, A.; Kiskinova, M.; Schlögl, R.; Salmeron, M. In Situ X-Ray Photoelectron Spectroscopy Studies of Gas-Solid Interfaces at near-Ambient Conditions. *MRS Bull.* **2007**, *32*, 1022−1030.
(46) Starr, D. E.; Liu, Z.; Hävecker, M.; Knop-Gericke, A.; Bluhm, H. Investigation of Solid/Vapor Interfaces Using Ambient Pressure X-Ray Photoelectron Spectroscopy. *Chem. Soc. Rev.* **2013**, *42*, 5833−5857.
(47) Stoerzinger, K. A.; Hong, W. T.; Crumlin, E. J.; Bluhm, H.; Shao-Horn, Y. Insights into Electrochemical Reactions from Ambient Pressure Photoelectron Spectroscopy. *Acc. Chem. Res.* **2015**, *48*, 2976−2983.
(48) Liu, Q.; Han, Y.; Cai, J.; Crumlin, E. J.; Li, Y.; Liu, Z. CO_2 Activation on Cobalt Surface in the Presence of H_2O: An Ambient-Pressure X-Ray Photoelectron Spectroscopy Study. *Catal. Lett.* **2018**, *148*, 1686−1691.
(49) Nenning, A.; Opitz, A. K.; Rameshan, C.; Rameshan, R.; Blume, R.; Hävecker, M.; Knop-Gericke, A.; Rupprechter, G.; Klötzer, B.; Fleig, J. Ambient Pressure XPS Study of Mixed Conducting Perovskite-Type SOFC Cathode and Anode Materials under Well-Defined Electrochemical Polarization. *J. Phys. Chem. C* **2016**, *120*, 1461−1471.
(50) Miller, D. J.; Øberg, H.; Kaya, S.; Sanchez Casalongue, H.; Friebel, D.; Anniyev, T.; Ogasawara, H.; Bluhm, H.; Pettersson, L. G. M.; Nilsson, A. Oxidation of Pt(111) under near-Ambient Conditions. *Phys. Rev. Lett.* **2011**, *107*, 195502.
(51) Yamamoto, S.; Bluhm, H.; Andersson, K.; Ketteler, G.; Ogasawara, H.; Salmeron, M.; Nilsson, A. In Situ X-Ray Photoelectron Spectroscopy Studies of Water on Metals and Oxides at Ambient Conditions. *J. Phys. Condens. Matter* **2008**, *20*, 184025.
(52) Dzara, M. J.; Artyushkova, K.; Shulda, S.; Strand, M. B.; Ngo, C.; Crumlin, E. J.; Gennett, T.; Pylypenko, S. Characterization of Complex Interactions at the Gas − Solid Interface with in Situ Spectroscopy: The Case of Nitrogen-Functionalized Carbon. *J. Phys. Chem. C* **2019**, *123*, 9074−9086.
(53) Artyushkova, K.; Matanovic, I.; Halevi, B.; Atanassov, P. Oxygen Binding to Active Sites of Fe−N−C ORR Electrocatalysts Observed by Ambient-Pressure XPS. *J. Phys. Chem. C* **2017**, *121*, 2836−2843.

https://dx.doi.org/10.1021/acs.jpcc.0c05244
J. Phys. Chem. C 2020, 124, 16529−16543

(54) Grosvenor, A. P.; Kobe, B. A.; Biesinger, M. C.; McIntyre, N. S. Investigation of Multiplet Splitting of Fe 2p XPS Spectra and Bonding in Iron Compounds. *Surf. Interface Anal.* **2004**, *36*, 1564−1574.
(55) Miedema, P. S.; de Groot, F. M. F. The Iron L Edges: Fe 2p X-Ray Absorption and Electron Energy Loss Spectroscopy. *J. Electron Spectrosc. Relat. Phenom.* **2013**, *187*, 32−48.
(56) Drevon, D.; Görlin, M.; Chernev, P.; Xi, L.; Dau, H.; Lange, K. M. Uncovering The Role of Oxygen in Ni-Fe(OxHy) Electrocatalysts Using In Situ Soft X-Ray Absorption Spectroscopy during the Oxygen Evolution Reaction. *Sci. Rep.* **2019**, *9*, 1−11.
(57) Giménez-Marqués, M.; Bellido, E.; Berthelot, T.; Simón-Yarza, T.; Hidalgo, T.; Simón-Vázquez, R.; González-Fernández, Á.; Avila, J.; Asensio, M. C.; Gref, R.; et al. GraftFast Surface Engineering to Improve MOF Nanoparticles Furtiveness. *Small* **2018**, *14*, 1801900.
(58) Heijboer, W. M.; Battiston, A. A.; Knop-Gericke, A.; Hävecker, M.; Bluhm, H.; Weckhuysen, B. M.; Koningsberger, D. C.; de Groot, F. M. F. Redox Behaviour of Over-Exchanged Fe/ZSM5 Zeolites Studied with in-Situ Soft X-Ray Absorption Spectroscopy. *Phys. Chem. Chem. Phys.* **2003**, *5*, 4484−4491.
(59) Ogletree, D. F.; Bluhm, H.; Hebenstreit, E. D.; Salmeron, M. Photoelectron Spectroscopy under Ambient Pressure and Temperature Conditions. *Nucl. Instrum. Methods Phys. Res., Sect. A* **2009**, *601*, 151−160.
(60) Bluhm, H.; Andersson, K.; Araki, T.; Benzerara, K.; Brown, G. E.; Dynes, J. J.; Ghosal, S.; Gilles, M. K.; Hansen, H.-C.; Hemminger, J. C.; et al. Soft X-Ray Microscopy and Spectroscopy at the Molecular Environmental Science Beamline at the Advanced Light Source. *J. Electron Spectrosc. Relat. Phenom.* **2006**, *150*, 86−104.
(61) Kishi, H.; Sakamoto, T.; Asazawa, K.; Yamaguchi, S.; Kato, T.; Zulevi, B.; Serov, A.; Artyushkova, K.; Atanassov, P.; Matsumura, D.; et al. Structure of Active Sites of Fe-N-C Nano-Catalysts for Alkaline Exchange Membrane Fuel Cells. *Nanomaterials* **2018**, *8*, 965.
(62) Wickramaratne, N. P.; Xu, J.; Wang, M.; Zhu, L.; Dai, L.; Jaroniec, M. Nitrogen Enriched Porous Carbon Spheres: Attractive Materials for Supercapacitor Electrodes and CO_2 Adsorption. *Chem. Mater.* **2014**, *26*, 2820−2828.
(63) Ngo, C.; Fitzgerald, M. A.; Dzara, M. J.; Strand, M. B.; Diercks, D. R.; Pylypenko, S. 3D Atomic Understanding of Functionalized Carbon Nanostructures for Energy Applications. *ACS Appl. Nano Mater.* **2020**, *3*, 1600−1611.
(64) Jaouen, F.; Lefèvre, M.; Dodelet, J.-P.; Cai, M. Heat-Treated Fe/N/C Catalysts for O_2 Electroreduction: Are Active Sites Hosted in Micropores? *J. Phys. Chem. B* **2006**, *110*, 5553−5558.
(65) Kumar, K.; Dubau, L.; Mermoux, M.; Li, J.; Zitolo, A.; Nelayah, J.; Jaouen, F.; Maillard, F. On the Influence of Oxygen on the Degradation of Fe-N-C Catalysts. *Angew. Chem.* **2020**, *132*, 3261−3269.
(66) Sun, Y.; Silvioli, L.; Sahraie, N. R.; Ju, W.; Li, J.; Zitolo, A.; Li, S.; Bagger, A.; Arnarson, L.; Wang, X.; et al. Activity-Selectivity Trends in the Electrochemical Production of Hydrogen Peroxide over Single-Site Metal-Nitrogen-Carbon Catalysts. *J. Am. Chem. Soc.* **2019**, *141*, 12372−12381.
(67) Luo, F.; Choi, C. H.; Primbs, M. J. M.; Ju, W.; Li, S.; Leonard, N. D.; Thomas, A.; Jaouen, F.; Strasser, P. Accurate Evaluation of Active-Site Density (SD) and Turnover Frequency (TOF) of PGM-Free Metal-Nitrogen-Doped Carbon (MNC) Electrocatalysts Using CO Cryo Adsorption. *ACS Catal.* **2019**, *9*, 4841−4852.
(68) Li, J.; Zhang, H.; Samarakoon, W.; Shan, W.; Cullen, D. A.; Karakalos, S.; Chen, M.; Gu, D.; More, K. L.; Wang, G.; et al. Thermally Driven Structure and Performance Evolution of Atomically Dispersed FeN_4 Sites for Oxygen Reduction. *Angew. Chem., Int. Ed.* **2019**, *58*, 18971−18980.
(69) Artyushkova, K. Misconceptions in Interpretation of Nitrogen Chemistry from X-Ray Photoelectron Spectra. *J. Vac. Sci. Technol., A* **2020**, *38*, 031002.
(70) Jablonski, A.; Powell, C. J. Relationships between Electron Inelastic Mean Free Paths, Effective Attenuation Lengths, and Mean Escape Depths. *J. Electron Spectrosc. Relat. Phenom.* **1999**, *100*, 137−160.
(71) Chen, Y.; Asset, T.; Lee, R.; Artyushkova, K.; Atanassov, P. Kinetic Isotopic Effect Studies of Iron-Nitrogen-Carbon Electrocatalysts for Oxygen Reduction Reaction. *J. Phys. Chem. C* **2019**, *123*, 11476−11483.
(72) von der Heyden, B. P.; Roychoudhury, A. N.; Mtshali, T. N.; Tyliszczak, T.; Myneni, S. C. B. Chemically and Geographically Distinct Solid-Phase Iron Pools in the Southern Ocean. *Science* **2012**, *338*, 1199−1201.
(73) Kumar, K.; Gairola, P.; Lions, M.; Ranjbar-Sahraie, N.; Mermoux, M.; Dubau, L.; Zitolo, A.; Jaouen, F.; Maillard, F. Physical and Chemical Considerations for Improving Catalytic Activity and Stability of Non-Precious-Metal Oxygen Reduction Reaction Catalysts. *ACS Catal.* **2018**, *8*, 11264−11276.
(74) Kim, H.; Lee, K.; Woo, S. I.; Jung, Y. On the Mechanism of Enhanced Oxygen Reduction Reaction in Nitrogen-Doped Graphene Nanoribbons. *Phys. Chem. Chem. Phys.* **2011**, *13*, 17505.
(75) Yao, Y.; Hu, Y.; Scott, R. W. J. Watching Iron Nanoparticles Rust: An in Situ x-Ray Absorption Spectroscopic Study. *J. Phys. Chem. C* **2014**, *118*, 22317−22324.
(76) Zitolo, A.; Ranjbar-Sahraie, N.; Mineva, T.; Li, J.; Jia, Q.; Stamatin, S.; Harrington, G. F.; Lyth, S. M.; Krtil, P.; Mukerjee, S.; et al. Identification of Catalytic Sites in Cobalt-Nitrogen-Carbon Materials for the Oxygen Reduction Reaction. *Nat. Commun.* **2017**, *8*, 1−10.

https://dx.doi.org/10.1021/acs.jpcc.0c05244
J. Phys. Chem. C 2020, 124, 16529−16543